University of Alberta

Large Black Holes in the Randall-Sundrum II Model

by

Shima Yaghoobpour Tari

A thesis submitted to the Faculty of Graduate Studies and Research
in partial fulfillment of the requirements for the degree of

Doctor of Philosophy

Department of Physics

To

All the individuals I have learnt something from throughout my life.

Abstract

The Einstein equation with a negative cosmological constant Λ in the five dimensions for the Randall-Sundrum II model, which includes a black hole, has been solved numerically. We have constructed an AdS_5-CFT_4 solution numerically, using a spectral method to minimize the integral of the square of the error of the Einstein equation, with 210 parameters to be determined by optimization. This metric is conformal to the Schwarzschild metric at an AdS_5 boundary with an infinite scale factor. So, we consider this solution as an infinite-mass black hole solution.

We have rewritten the infinite-mass black hole in the Fefferman-Graham form and obtained the numerical components of the CFT energy-momentum tensor. Using them, we have perturbed the metric to relocate the brane from infinity and obtained a large static black hole solution for the Randall-Sundrum II model. The changes of mass, entropy, temperature and area of the large black hole from the Schwarzschild metric are studied up to the first order for the perturbation parameter $1/(-\Lambda_5 M^2)$. The Hawking temperature and entropy for our large black hole have the same values as the Schwarzschild metric with the same mass, but the horizon area is increased by about $4.7/(-\Lambda_5)$.

Figueras, Lucietti, and Wiseman found an AdS_5-CFT_4 solution using an independent and different method from us, called the Ricci-DeTurck-flow method. Then, Figueras and Wiseman perturbed this solution in a same way as we have done and obtained the solution for the large black hole in the Randall-Sundrum II model. These two numerical solutions are the first math-

ematical proofs for having a large black hole in the Randall-Sundrum II. We have compared their results with ours for the CFT energy-momentum tensor components and the perturbed metric. We have shown that the results are closely in agreement, which can be considered as evidence that the solution for the large black hole in the Randall-Sundrum II model exists.

Acknowledgements

This thesis is the result of four years of work and life experience at the University of Alberta, Edmonton. Through these four years, I was far away from my beloved family, but there have been individuals in my life who have helped, encouraged, and supported me to keep going and make this work possible.

I would express my sincere gratitude to my supervisor, Professor Don N. Page, for his support and for being there whenever I needed his guidance. I wish that I could be as devoted and curious as he is toward science. It is always great to see Don's eagerness to express his ideas and understandings. Through working with Don, I have learnt that you can trust and try your simple ideas to solve the difficult problems.

I would like to thank Professor Valeri P. Frolov as a wonderful teacher. It was a great experience to attend his classes. His perfect way of teaching and explaining the complicated concepts shall always inspire me.

I would like to extend my acknowledgement to Professor Sharon Morsink for listening to me whenever I needed her help, advice and support.

I thank my committee members Professor Dmitri Pogosyan, Professor Vincent Bouchard, and Dr. Toby Wiseman for taking their time to read my thesis and provide me with their useful comments.

I would like to express my appreciation for my collaborators, Céline and Shohreh. Thanks Céline for your great contribution and significant work for the computational part of the project. Thanks Shohreh for your persistence through the work. I have learnt many technical things from both of them

through the work.

I would like to gratefully acknowledge the kindness of Pau Figueras, James Lucietti, and Toby Wiseman in giving us their detailed results.

I would like to express my thankfulness to Sarah Derr for her great advice and to Dr. Isaac-Yakoub Isaac for helping me to have extra hours of TA, which was helpful financial aid for me. I would like to extend my thanks for Sandra Hamilton, Linda Jacklin, and Nandi Khana for their help and kindness.

When you are far away from home, having good friends and people around you makes your life happier and easier. Thanks Shiva for being my best friend and sharing your time with me in the good and bad moments for three and a half years in Edmonton. I always admire your honesty and good taste. Thanks Neda for your kindness and friendship. Your home was the only home in Edmonton that I felt so comfortable to go to whenever I liked and needed a friend to enjoy my time with. Thanks Giang for all the joyful moments we had together. Your smile is always a wonderful image in my mind. Thanks Lan for the great experiences we had together as roommates. Thanks Prado for your short presence in my life, but for your great impact as a strong and intelligent girl. Thanks Mina for your kindness.

I do not have my Iranian family around in Edmonton, but I have a wonderful Canadian family here. I cannot express my appreciation in words for Marjie and Phil. I am so thankful that you let me be a part of your life. I feel so comfortable with you in your home environment in order to completely be myself, to laugh with you as hard as I can until rolling on the ground, and to let my tears come down whenever I need to cry. Your help, encourage-

ment, and unconditional love is so valuable for me. I have learnt great things through living with you. My special thanks to Marjie for doing her best to make an ideal and perfect New Year's ceremony for me during the past three years in their home. I can never forget that you were beside me all those times to do all the preparations. You will be with me all my New Years from now on, even if we can not be together physically. Thanks Phil for feeding Fat Albert and the boys (my fish for New Year).

I owe Shadi my special thanks for thousands of things. She is the one whose presence in my life as a best friend helps me to know myself better. Thanks Shadi for all the time that we shared together in happy, sad, and ordinary moments. It is a great feeling that I can be sure that I have someone whom I can count on when I am in need, even though she is living far from me. Our friendship has grown through the past 11 years, and I have learnt lots of things from her.

My father and my brother are the most important men in my life. Their presence in my life is always heartwarming for me, because of their unconditional love and support for me. Thanks Amir Mohammad for all the good feeling that we experience together. With you, I have learnt how life can be peaceful and enjoyable with someone whom you love, even if both of you live in completely different worlds. Thanks Dad (Baba) for all great things that you have provided for me and for tolerating all the time that we are missing being together. I know how hard it is for you.

I would like to express my sincere thanks to my mother. Thanks Mom (Maman) for all 1460 days when you called me every morning to remind me how much you love me and support me in all kinds of circumstances. During

the days I have been away from you, it has happened many times that I was so thankful for having you beside me in my life to teach me good qualities like being strong, independent, and enjoying my life as much as I can. I appreciate your presence in my life not only because you are my mom but as a great human being to teach me how to live.

Table of Contents

List of Tables

List of Figures

Chapter 1

Randall-Sundrum as a Braneworld Model

Most of the current theories in gravity are aimed to unify gravity with other fundamental forces and particles in nature. One of the candidates is string theory, with the principal assumption that the spacetime is a higher-dimensional one while we are living in a four-dimensional spacetime. So we need to assume extra spatial dimension(s) for these theories.

From an historical point of view, Nordström [49] was the first one who proposed the idea of an extra dimension in 1914. In his work, he showed that one could unify gravity with electromagnetism by assuming an extra spatial dimension. After Einstein published his general relativity theory, Kaluza [34] and Klein [39] suggested the first five-dimensional model to unify gravity and electromagnetism, working in the Einstein general relativity framework with one compactified extra dimension.

Another higher-dimensional model is the braneworld model. The first

braneworld model was proposed in 1998 by Arkani-Hamed, Dimopoulos, and Dvali [4, 5], known as the ADD model, based on Rubakov and Shaposhnikov's idea, proposed in 1983 [54]. It is a six-dimensional model, with two flat compactified extra dimensions, to solve the hierarchy problem. It should be mentioned that the ADD model requires at least two extra dimensions, but it can have more than two. Other braneworld models were proposed for solving the hierarchy problem by Randall and Sundrum, known as RSI [52], and RSII [53]. The RS model is a warped five-dimensional braneworld model with an extra dimension that can be large and not compactified for the RSII.

In this chapter, we review the basic definition and geometric formalism for the braneworld model [45, 51, 56, 61]. Then, we focus on the Randall-Sundrum models and their characteristics.

1.1 Braneworld Model

1.1.1 Definition

The braneworld model includes a higher-dimensional spacetime that is called the bulk and a lower-dimensional spacetime called the brane, which is embedded in the bulk. All matter and fields in the standard model are supposed to propagate on the subspace manifold, the brane, but gravity is the only force that can propagate through the whole space, the bulk. In the braneworld model, our four dimensional universe is considered as a 3-brane, which is a 1+3 hypersurface, surrounded by a higher-dimensional spacetime.

From the geometric aspect, the brane is a hypersurface that is embedded in a bigger space and can evolve in time. We can relate the geometry of

a spacetime and the surface within it, since the embedding will affect the geometry of the surface. In the braneworld, a singular distribution of energy-momentum tensor is a characteristic of the brane. This makes the mass-energy distribution confined to the brane as a surface rather than the bulk as the full spacetime. So, instead of having a nonsingular energy-momentum tensor that has units of energy per volume of the bulk spatial volume, it has units of energy per volume of the brane spatial volume. In some special cases there is a symmetry in the model as well, which makes the brane as a set of fixed points of that symmetry.

For the next section, we try to go through the geometric formalism for the braneworld model, specifically for the five-dimensional model. We will see how the geometric character of the spacetime can be described with the singularity characteristic of the energy-momentum tensor in the braneworld.

1.1.2 Geometry for the Braneworld Model

The bulk, the manifold $\mathbf{M}$, has the coordinate system $\{x^A\}$, with $A = 0, 1, 2, 3, 4$ for the five-dimensional spacetime, and the metric g_{AB}. The brane, a submanifold $\mathbf{S}$, is a hypersurface or surface of codimension one, a $3 + 1$-dimensinal surface in the five-dimensions, with an intrinsic coordinate system $\{y^a\}$ with $a = 0, 1, 2, 3$. The line element on the brane can be described by the metric h_{ab} as

$$h_{ab} = g_{AB}e_a^A e_b^B. \tag{1.1}$$

This is called the induced metric or the first fundamental form of the hypersurface. $\{e_a^A\}$ are the projection operators defined as

$$e_a^A = \frac{\partial x^A}{\partial y^a}. \tag{1.2}$$

They are tangent vectors on the brane.

We can describe the hypersurface with an equation $\phi(x^A) = 0$. Then the unit normal vector for the timelike hypersurface, n_A, can be defined as

$$n_A = \frac{\phi_{,A}}{|g^{BC}\phi_{,B}\phi_{,C}|^{\frac{1}{2}}}, \tag{1.3}$$

so $e_a^A n_A = 0$. We consider the case in which the gradient of ϕ is spacelike at $\phi(x^A) = 0$, so the n_A is spacelike as well. Then the normal vector points in the direction of increasing ϕ.

The inverse of the induced metric, the intrinsic metric for the hypersurface, can be determined by

$$h^{AB} \equiv h^{ab}e_a^A e_b^B = g^{AB} - n^A n^B. \tag{1.4}$$

We shall calculate whether the covariant derivative on the bulk, defined as ∇_A, differs from the covariant derivative on the brane, defined as D_a. We restrict our calculation to a tangent vector field, V^A, where $V^A = V^a e_a^A$, so $V^A n_A = 0$.

The definition for D_b, as an intrinsic covariant derivative, is the projection

of $\nabla_B V_A$ on the hypersurface, so

$$D_b V_a \equiv \nabla_B V_A e_a^A e_b^B. \tag{1.5}$$

By doing some calculation, it can be shown that the right hand side of (1.5) is $V_{a,b} - \Gamma_{ab}^c V_c$, which is the known expression for the covariant derivative with

$$\Gamma_{ab}^c = \frac{1}{2} h^{cd} (h_{ad,b} + h_{bd,a} - h_{ab,d}). \tag{1.6}$$

Now, we try to find the components of the vector $\nabla_B V^A e_b^B$ to see its tangential and normal components on the hypersurface. $\nabla_B V^A e_b^B$ can be written as $g_C^A \nabla_B V^C e_b^B$ and g_C^A can substitute with (1.4), so

$$
\begin{aligned}
\nabla_B V^A e_b^B &= (n^A n_C + h^{ac} e_a^A e_{Cc}) \nabla_B V^C e_b^B \\
&= (n_C \nabla_B V^C e_b^B) n^A + h^{ac} (\nabla_B V^C e_b^B e_c^C) e_a^A.
\end{aligned}
\tag{1.7}
$$

Vector V^C is a tangent vector on the hypersurface; therefore $n_C V^C = 0$. Then $n_C \nabla_B V^C = -V^C \nabla_B n_C$. Using (1.5), we have

$$\nabla_B V^A e_b^B = h^{ac} (D_b V_c) e_a^A - V^c (\nabla_B n_C e_c^C e_b^B) n^A. \tag{1.8}$$

If we define

$$K_{ab} \equiv \nabla_B n_A e_a^A e_b^B, \tag{1.9}$$

then

$$\nabla_B V^A e_b^B = D_b V^a e_a^A - V^a K_{ab} n^A. \tag{1.10}$$

K_{ab} is called the extrinsic curvature or second fundamental form, which is the normal component of the bulk covariant derivative of a tangent vector on the hypersuface. K_{ab} is a symmetric tensor, $K_{ab} = K_{ba}$. We can write the extrinsic curvature as

$$K_{ab} = \frac{1}{2}(\pounds_n g_{AB})e_a^A e_b^B, \tag{1.11}$$

where $\pounds$ is the Lie derivative.

As it was shown, the extrinsic curvature K_{ab} is an extrinsic feature of the hypersurface which measures the bending of the hypersurface, the brane, in the spacetime manifold, the bulk, while the induced metric, h_{ab}, is an intrinsic feature of the brane. By means of these tensors we can determine other geometrical aspects of the hypersurface.

Next, we want to find the relation between the Riemann tensor in the bulk and the same tensor on the brane in terms of the extrinsic curvature and the induced metric. The intrinsic curvature tensor by using the covariant derivative on the hypersurface is written as

$$D_a D_b V^c - D_b D_a V^c = -R^c{}_{dab} V^d. \tag{1.12}$$

R^c_{dab} has the same form that we know for the Riemann tensor in terms of the Γ^c_{ab} in (1.6) and its derivatives. The following quantity,

$$\nabla_B \nabla_C e_a^A e_b^B e_c^C - \nabla_C \nabla_B e_a^A e_b^B e_c^C = -R^A{}_{DCB} e_a^D e_c^C e_b^B, \tag{1.13}$$

is the one that we need to calculate in order to find the required relation. Considering (1.10), if we put $V^A = e_a^A$, then for a timelike hypersurface we

have

$$\nabla_B e_a^A e_b^B = \Gamma_{ab}^c e_c^A - K_{ab} n^A. \tag{1.14}$$

After doing some algebra, the projection of the Riemann tensor for the bulk on the hypersurface is given by the following relation:

$$R^A_{\ BCD} e_A^a e_b^B e_c^C e_d^D = R^a_{\ bcd} + (K_d^a K_{bc} - K_c^a K_{bd}). \tag{1.15}$$

This equation is called the Gauss equation.

The projection of the Riemann tensor for the bulk along the normal vector of the hypersurface will give us

$$R_{ABCD} n^A e_b^B e_c^C e_d^D = D_d K_{bc} - D_c K_{bd}. \tag{1.16}$$

This equation is called the Codazzi equation. We can see that the bulk curvature can be expressed in terms of the brane curvature and the extrinsic curvature and its derivative. So even here, we can see the effect of the embedding of the brane in the bulk.

The Einstein tensor for the bulk, $G_{AB} = R_{AB} - \frac{1}{2} R g_{AB}$, includes the following parts:

$$-2 G_{AB} n^A n^B = {}^b R + (K^{ab} K_{ab} - K^2), \tag{1.17}$$

$$G_{AB} e_a^A n^B = D_b K_a^b - D_a K, \tag{1.18}$$

using the contracted form of the Gauss-Codazzi equations. ${}^b R = h^{ab} R_{acb}^c$ is the Ricci scalar for the brane, and $K \equiv h^{ab} K_{ab} = \nabla_A n^A$. The Gauss-Codazzi

equations gives us part of the Einstein equations on the brane, which we need to work with. The remaining part $G_{AB}e_a^A e_b^B$ cannot be written only in terms of h_{ab} and K_{ab}; it involves the Lie derivative of K_{ab} in the n direction.

The brane, as a hypersurface, splits the space into two regions. We want to see how this affects our quantities in the both regions while we jump across the hypersurface from one region to the other one. We have two regions of the spacetime, M^+ and M^-, which have a common boundary, the hypersurface, **S**. The metric on M^+ is g_{AB}^+ with coordinate system x^{A+}, and the metric on M^- is g_{AB}^- with the coordinate system x^{A-}. The following definition will be helpful throughout the rest of the explanation:

$$[V] \equiv V(M^+)|_S - V(M^-)|_S, \tag{1.19}$$

where V is our tensorial quantity, and calculating $[V]$ shows the change of the quantity when we jump from one region to another one. The unit normal vector, n^A, points from M^- to M^+. The value of $[n^A]$ and $[e_a^A]$ are zero. As mentioned, the induced metric and the extrinsic curvature are the characteristics of the hypersurface, so we need to check the $[V]$ for them. Applying $[V]$ for h_{ab} gives

$$[h_{ab}] = 0. \tag{1.20}$$

Eq. (1.20) is called the first junction condition. This means that both metrics g_{AB}^+ and g_{AB}^- induce the same metric on the hypersurface. This is the required condition in order to have a well-defined hypersurface.

For $[K_{ab}]$, the condition is different. It happens that $[V]$ in (1.19) is not zero but can be described by the stress-energy tensor on the hypersurface.

We consider the stress-energy tensor of the hypersurface as

$$T_S^{AB} = S^{ab} e_a^A e_b^B \, |g^{CD} \phi_{,C} \phi_{,D}|^{\frac{1}{2}} \delta(\phi), \qquad (1.21)$$

where, as mentioned, $\phi = 0$ is the equation of the hypersurface. If we do an integral for the Einstein equation, $G_{AB} = \kappa_5^2 T_{AB}$, around the hypersurface including both regions and using (1.17) and (1.18), we can derive that

$$[K_{ab}] = \kappa_5^2 (S_{ab} - \frac{1}{3} h_{ab} S). \qquad (1.22)$$

This is called the second junction condition. This junction condition is known as the Israel junction condition [33]. Here, we can see that the energy-momentum singularity can be related to the jump of the extrinsic curvature through the brane as a geometric aspect of the spacetime.

All the mentioned quantities and the relations are covering the geometry and dynamics of the braneworld. For the next section, we will have a review on the Randall-Sundrum model and see how we can apply these relations for the Randall-Sundrum model as an example of the braneworld.

1.2   The Randall-Sundrum Model

In 1999, Randall and Sundrum [52, 53] proposed two of the first braneworld models with a negative cosmological constant for the bulk metric, which at-tracted a lot of attention. As mentioned, the standard model fields are con-fined to the brane in the braneworld. The role of the five-dimensional cosmo-logical constant is to balance the effects of the four-dimensional sources in five

dimensions, in order to have a flat brane. It is quite different from the role of the four-dimensional cosmological constant. Assuming the five-dimensional cosmological constant results in having a curved five-dimensional background, we can still keep our brane flat by introducing the curved extra dimension(s) in a warped extra-dimension model so that the four-dimensional cosmological constant vanishes [54].

The Randall-Sundrum model (RS) was proposed in two types, RSI and RSII. RSI [52] has two branes with negative and positive tensions and for RSII, the brane with negative tension was sent to the infinity. The metric and basic characteristics for the RS models will be explained in the following lines.

1.2.1   RSI

For RSI, we are looking for an Einstein equation solution for a five-dimensional bulk enclosed with two 3-branes, one of which should look like our world. We assume that our extra dimension is compactified, defined as a S^1/Z_2 orbifold, where S^1 is a one-dimensional sphere (a circle) and Z_2 is the multiplicative group of $\{-1, 1\}$. It would fix two points along the extra dimension y, $y = 0$ and $y = \pi R = L$, which are locations for the two 3-branes. In addition, we want our four-dimensional brane to be flat and static. Fig.(1.1) shows the schematic set-up for the RS model. An ansatz metric that would satisfy above criteria has the following form as

$$ds^2 = e^{-2A(y)}\eta_{ab}dx^a dx^b + dy^2. \tag{1.23}$$
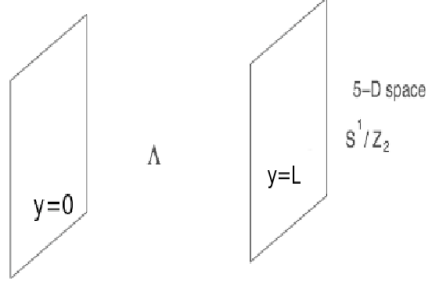
Figure 1.1: The schematic set-up for the RS model (taken from [9])

Here η_{ab} is the metric for Minkowski space-time and $e^{-2A(y)}$ is the warp-factor, depending only on the extra dimension coordinate y that makes the metric non-factorizable. After defining the general form of the metric, we need to find $A(y)$ for the metric, which needs to be a solution of the five-dimensional Einstein equation as $G_{AB} = \kappa_5^2 T_{AB}$. $\kappa_5 \equiv \frac{1}{M_5^3}$, where M_5 is the five-dimensional Planck mass scale.

Assuming a five dimensional AdS bulk with a positive tension brane on AdS boundary and a negative tension brane without any matter on the brane can be described by the following Einstein-Hilbert action

$$S = \int dy d^4\vec{x} \sqrt{-^5g}\, (M_5^3 R - \Lambda_5) - \int dy d^4\vec{x} \sqrt{-^4h}\, (\lambda_+ \,\delta(y) + \lambda_- \,\delta(y - L)).$$

(1.24)

Here ^4h is the determinant of the four-dimensional metric induced from the five dimensional metric $^5g_{AB}$ with determinent ^5g for the $y = $ constant brane and Λ_5 is the five dimensional cosmological constant. The gauge is chosen in a way that branes are located at $y = 0$ and $y = L$. The action S depends on

the five dimensional metric, its derivatives, which is included in Ricci scalar, and the four dimensional metric induced on the brane, which is induced from the five dimensional metric. For the general case, we can have a matter field localized on the brane, but for the action (1.24), it is assumed that there is no matter fields. Solving the Einstein equation for G_{55} gives

$$6A'^2 = -\frac{\Lambda_5}{2M_5^3},\tag{1.25}$$

A' is defined as the derivative of $A(y)$ with respect to the y. (1.25) implies that Λ_5 should be negative to have a real solution, so we have an AdS_5 model. We impose the Z_2 symmetry, which makes the two sides of the brane mirror images of each other and define k^2 as $-\frac{\Lambda_5}{12M_5^3}$. This gives us $A(y) = k|y|$, so the complete form of the metric (1.23) is

$$ds^2 = e^{-2k|y|}\eta_{ab}dx^a dx^b + dy^2,\tag{1.26}$$

for $-L \leqslant y \leqslant L$. The Z_2 symmetry about the brane is incorporated with the $|y|$ term. We can see that under this symmetry, acting on coordinates like $(x^a, y) \longrightarrow (x^a, -y)$, the metric is invariant. We also apply a Z_2 symmetry about the brane at $y = L$, even though that is not directly implied by the form of the metric (1.26). The metric (1.26) is the RSI metric in the simplest form. It can be shown that even if η_{ab} is substituted by any vacuum solution of the Einstein equation in four dimensions, the resulting metric still would be a solution for the RS model in five dimensions.

Solving the Einstein equation for the G_{ab} components and considering that

the Israel junction condition [33] should be satisfied on the branes imply that

$$\lambda_+ = -\lambda_- = 12kM_5^2. \tag{1.27}$$

Calculating the extrinsic curvature for the metric on the both sides of the brane at $y = 0$ for $y \longrightarrow 0^+$ and $y \longrightarrow 0^-$ shows that $[K_{ab}] \neq 0$. So, the space-time is singular at the brane. Using the five-dimensional Einstein equation, $G_{AB} = \kappa_5^2 T_{AB}$, gives us the energy-momentum tensor as

$$\kappa_5^2 T_{AB} = -\Lambda_5 \ g_{AB} - 6ke_A^a e_B^b \eta_{ab}(\lambda_+\delta(y) + \lambda_-\delta(y - L)). \tag{1.28}$$

In our case we assume zero stress-energy tensor on the brane, except for a Lorentz-invariant brane tension or cosmological constant tuned to the value that would allow the brane to be the flat Minkowski metric in the AdS$_5$ bulk. Thus, we can see that the spacetime singularity on the brane is related to the energy-momentum tensor on the brane and can be considered as the brane tension.

We can perturb the action (1.24) around our background metric η_{ab}. For a perturbed metric $g_{ab}^{(0)}$ defined as $\eta_{ab} + \epsilon_{ab}^{(0)}$, the term related to the four dimensional action is

$$S \supset M_5^3 \frac{(1 - e^{-2kL})}{k} \int d^4\vec{x} \ \sqrt{-g^{(0)}} \ \ ^bR, \tag{1.29}$$

where ^bR is the four-dimensional Ricci scalar on the brane. From this action, we can find the relation between the Planck mass M_{Pl} in four dimensions and

the five-dimensional Planck mass M_5 scale as

$$M_{Pl}^2 = (1 - e^{-2kL})\frac{M_5^3}{k}.$$ (1.30)

The brane with the negative tension at $y = L$ is the one that has the standard model confined on it. It can be shown that by adjusting $kL \approx 35$, we can have the energy scale on this brane around 1 TeV. Therefore, this brane is called the TeV brane. The energy scale for the brane with positive tension is around the Planck scale, so it is called the Planck brane. We can see that the energy hierarchy can be absorbed from the Planck brane toward the TeV brane. So, the first RS model provides a solution for the hierarchy problem.

1.2.2   RSII

We take the limit as $L \longrightarrow \infty$ for the RSI metric (1.26). This means that the negative tension brane would be sent to infinity, and we have one brane with positive tension in RSII. It is supposed that we are living on this brane. We introduce the coordinate transformation for y to z, defined by the function $z \equiv sgn(y)(e^{k|y|} - 1)/k$. After applying this transformation for the metric, we have

$$ds^2 = \frac{1}{(k|z| + 1)^2}(\eta_{ab}dx^a dx^b + dz^2).$$ (1.31)

This metric is a conformally flat metric. In this case, the Planck mass is derived as $M_{Pl}^2 = \frac{M_5^3}{k}$, so we do not have an explanation for hierarchy problem in RSII. In figure (1.2), the schematic plot for RSII is shown.

The behavior of gravity around the brane can be studied in RSII. The
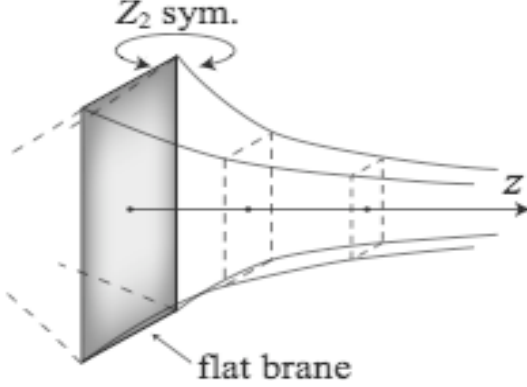
Figure 1.2: The schematic plot for the RSII model (taken from [58])

metric can be rewritten as

$$ds^2 = g^{(0)}_{AB}dx^A dx^B. \tag{1.32}$$

Now, we can perturb the metric $g^{(0)}_{AB}$ and define the perturbed metric as $g_{AB} \equiv g^{(0)}_{AB} + h_{AB}$. We will work in an RS gauge where [58]

$$h_{55} = h_{a5} = 0 \ , \qquad \partial^a h_{ab} = 0 \ , \qquad h^a_a = 0. \tag{1.33}$$

After considering all the conditions, the equation of motion for the perturbed metric is

$$[-\partial_z^2 + V(z)]\psi_{ab} = \eta^{cd}\partial_c\partial_d\psi_{cd}, \tag{1.34}$$

where $\psi_{ab} \equiv \sqrt{|z| + 1/k} \ h_{ab}$ and $V(z) = \frac{15k^2}{4(k|z|+1)^2} - 3k\delta(z)$. $V(z)$ can be considered as a volcano type gravitational potential as a result of the brane presence. Assuming $\psi_{ab} \propto \hat{u}_m(z) \ e^{iK_c x^c}$, to make the variable separated, gives us

$$[-\partial_z^2 + V(z)]\hat{u}_m(z) = m^2 \ \hat{u}_m(z), \tag{1.35}$$

where $m^2 = -K_a K^a$, and m is the four-dimensional mass for the $\hat{u}_m(z)$ mode. Equation (1.35) is a Schrödinger-like equation that can be solved to find the different gravitational mass around the brane. We should choose solutions that satisfy the Z_2-symmetry around the brane (the review for solutions is given in [53]). Finding all gravitational modes leads us to find the perturbed metric around the brane at $y = 0$. The behavior of the modes shows that the higher-dimensional gravity is localized around the brane, despite the fact that the extra dimension is extended to infinity. We can calculate the gravitational potential for different mass on the brane, see [53, 23]. From that, we can conclude that the four-dimensional theory of gravity is recovered on the brane.

From a different point of view, the Einstein equations for the RS model on the brane is derived in [56]. The result shows that the Einstein equation in four-dimensions in the low-energy limit is recovered on the brane world. Using the derived equation shows that the negative brane in RSI does not have the right signature for gravity, but the RSII model does.

Therefore, having all those results for RSII shows that it can be a good candidate for a braneworld model in higher dimensions to be studied.

Chapter 2

Black Holes in the RS II Braneworld Model

The study of black holes in higher dimensions attracts much attention for theoretical physicists for different reasons regarding to the application for their work.

From a mathematical point of view, we are dealing with more complicated theories. First, we can consider different kinds of black objects in higher dimensional with different features to study. Studying the higher-dimensional black hole spacetime shows that the horizon topology is different from the four-dimensional one, which is S^2. The first vacuum solution for a spherically symmetric black hole in higher dimensions is the Tangherlini metric with horizon topology S^{D-2} [60]. We can generalize this and add a $D-N$ flat spatial line element to the black hole solution of the N-dimensional Einstein equation in vacuum with horizon topology S^{N-2}. This black hole solution is called a black brane with horizon topology defined as $S^{N-2} \times R^{D-N}$, and if $D = N+1$

it is called a black string [22]. On the other hand, for the rotating black holes, we have more parameters to work with, since the higher are the dimensions for a rotating black hole, the more are the independent components of the angular momentum [48].

From an applicational point of view, the following reasons can be mentioned for studying black holes in higher dimensions. First, producing the higher-dimensional black hole in colliders is predicted by Giddings and Thomas in [24] for the first time, which could be considered as a experimental proof for one or more extra dimensions if such black holes are ever observed. A good review on the subject can be found in [7, 35], written by Caviglia and Kanti. Second, the first achievement to derive the Bekenstein-Hawking area-entropy relation in string theory has been done for a five-dimensional black hole [57]. Therefore, we can consider the higher-dimensional black hole to examine how the string theory, as a potential candidate for quantum gravity, works for black holes. And, there are many other reasons to encourage us to investigate more about the higher-dimensional black holes. A good and complete review on black holes in higher dimensions can be found in [14].

Studying the braneworld model, as a higher-dimensional model, shows that the four-dimensional weak gravity can be recovered on the brane. But, the strong gravity, especially black holes, is hard to study because of the difficulty for solving the Einstein equation.

For the braneworld model, we expect to have the energy scale at the TeV scale for gravity on the brane. The possibility of creation of a small black hole in high-energy colliders is predicted in [10] for the compact braneworld model, ADD. Small black holes can be defined as black holes which have their

horizon radii smaller than the size of the extra dimension. In [20, 21] it was showed that the black hole in the braneworld model may escape from the brane as a recoil. It was explained as an interaction between the brane and the small black hole in the context of a field theory model, in which a black hole can be described as a massive scalar.

For a braneworld model with a compactified extra dimension and asymptoting to $M^d \times S^1$, where M^d is the d-dimensional Minkowski spacetime, we have two types of black hole with different horizon topologies in our theory, called the Kaluza-Klein theory. These black objects are classified as localized black holes in the bulk and as black strings. For a localized black hole, the solution for $d = 3$ is derived in [19, 6], and for $d \geq 4$, the numerical solution for the Schwarzschild black hole has been constructed in [42].

The homogeneous black string metric can be defined as

$$ds^2 = h_{ab}dx^a dx^b + dy^2, \tag{2.1}$$

where h_{ab} is considered as a black hole solution in d-dimensions and y as the coordinate in the same direction as the S^1. But, according to the Gregory-Laflamme instability explained in [27, 28], when the radius of the horizon is smaller than the length of the S^1, the black string solutions can be unstable. Considering this fact, the properties of the black string are studied analytically and numerically. A review on Kaluza-Klein black holes can be found in [31].

Turning to the RSII braneworld model, we can consider the model as an explanation for having our universe as its domain wall while including the extra dimension. Therefore, finding an astrophysical-size black hole solution

on the brane is desirable. Many attempts have been made to find the large black hole solution for RSII, both analytic and numeric. However, no solution for this kind has been found until recent works of [16, 17] and our work, which will be explained in the next chapters. There are conjectures for the existence or non-existence for the large black hole and some numerical approach for the small black hole in RSII. In this chapter, we will review these works.

2.1   Analytical Attempts for Finding a Black Hole in RSII

The first attempt to find a black hole in RSII has been done in [8]. One may consider the metric

$$ds^2 = \frac{l^2}{z^2}\bigg(dz^2 + h_{ab}dx^a dx^b \bigg), \tag{2.2}$$

where l is the AdS radius. h_{ab} can be any Ricci-flat metric in order that (2.2) satisfies the Einstein equation with the negative cosmological constant. Therefore, substituting the Schwarzschild metric for h_{ab} gives us a black string with a warp factor in the RSII model.

For this solution, the Ricci scalar and the square of the Ricci tensor are finite everywhere, but the square of the Riemann tensor is proportional to z^4/r^6, where r is the radial coordinate. Therefore, it diverges at $z \to \infty$, where the AdS horizon is located, and it is singular at $r = 0$. On the other hand, the radius of the black string shrinks as we move from the brane to infinity, so the solution is unstable according to the Gregory-Laflamme insta-

bility [27, 28]. Therefore, this black string solution cannot be considered as a static black hole.

In addition to the black string (2.2), other attempts to find the exact five-dimensional black object solution have also failed. However, Emparan et al. [13] constructed an exact black hole solution for the RSII model in four dimensions, where we have an AdS_4 bulk and $(2+1)$-dimensional brane. The metric is constructed from an AdS C-Metric, which is an accelerating black hole solution for the Einstein equation [38, 50]. The authors suggested that an exact solution for a black hole on a 3-brane may be found by using the analog of the C-metric in five dimensions. But, such solution has not been found yet.

It is hard to find an exact solution for the black object in RSII. Despite this fact, in [37] an exact brane-localized black hole has been found in the near-horizon region as an extremal black hole. The near-horizon geometrical analysis [43] has been applied, which simplifies the problem because of the symmetries. This reduces the bulk Einstein equation to a regular ODE to be solved. But, even the existence of this solution would not ensure that there can be a static black hole solution for the whole bulk.

Some other attempts have been done to find a black hole in RSII analytically, using perturbation. The first example was constructed by Karasik et al. [36], using matched asymptotic expansions, but they were actually inconclusive over whether the solution existed.

Therefore, we can conclude that no analytical solution for a five-dimensional static black object in RSII was found until recently, as will be reported below.

2.2 Application of AdS/CFT Correspondence for the Black Hole in RSII

Assuming the AdS/CFT correspondence [3, 46] for the braneworld, we can describe physics in the bulk of an AdS space-time by a conformal field theory living on the brane as the boundary. So, solving the $D+1$-dimensional classical equations for the bulk is equivalent to solving the D-dimensional gravity coupled to strongly coupled conformal fields, which means $G_{\mu\nu} = 8\pi G_D \langle T_{\mu\nu} \rangle_{CFT}$. According to [11], the conjecture holds for strong gravity on the brane as well. Then, the dynamics of the black hole derived by solving the bulk equations in $D+1$-dimensions classically corresponds to the dynamics of the D-dimensional quantum-corrected black holes on the brane, which is described by considering the conformal field theory plus gravity. For the Randall-Sundrum model, the brane is the boundary of the asymptotically AdS bulk, and we can apply the AdS/CFT correspondence to study the existence of the black hole in the model. It is only a conjecture to assume that the AdS/CFT correspondence holds, since it is hard to solve the problem on both sides to check whether it really works in this case or not.

Emparan and et al. [11] and Tanaka [59] assumed that AdS/CFT holds so that CFT in the large N limit is used to study the quantum effects of the black hole localized on the brane. N is defined as $\frac{l}{l_{Pl}}$, where l is the AdS radius and l_{pl} is the Planck length. The conformal symmetry for the CFT at the IR regime on the brane is valid, so we have no mass gap, and any finite temperature black hole can emit CFT modes as Hawking radiation. In this description, they considered that the effective degrees of freedom is $O(N^2)$

so as mentioned the large number of CFT modes are involved and the black hole is considered as a huge source of radiation which accelerates the mass loss and makes the lifetime of the black hole short.

A brane observer would see a four dimensional black hole on the brane with quantum correction which makes the area decrease due to the Hawking radiation, while the bulk observer would see the deformation of the geometry in the bulk as classical evaporation of a five-dimensional black hole. So, it is concluded that there is no static black hole solution in RSII. The other point that should be considered is that the AdS/CFT correspondence may not be valid where the black hole radius is as small as the AdS radius, l, since the CFT modes in the UV regime must be considered as the bulk graviton and they can not be used as dual CFT degrees of freedom. So, the evolution of a small black hole may not be correctly explained by applying the AdS/CFT correspondence.

To sum-up, these groups deduced that there is no large static black hole in RSII by assuming that AdS/CFT holds for the model.

In reference [18], Fitzpatrick, Randall, and Wiseman give an example and a reasoning that the above argument in [11] and [59] may not be justified. First, they point out that the black string defined by the metric (2.2) is an example for the static quantum corrected black hole for h_{ab} defined as the Schwarzschild black hole, in contrast to what is in reference [11] and [59] where the authors claimed that there is no static black hole. For this example, the induced metric on the brane is exactly the four-dimensional Schwarzschild metric solution, so there is no place for the QFT contribution to the energy-momentum tensor and no backreaction effect from the CFT is

available. However, we know that the black string is unstable.

The second point is that the argument in [11] and [59] depends on the weak coupling calculation by applying the free field theory idea to the CFT, while according to the AdS/CFT conjecture, the CFT is a strongly coupled field theory on the brane correspondence to the bulk solution. Considering that the CFT at large 't Hooft coupling cannot be solved, a heuristic method is used by applying a confinement mechanism. Then, it is shown that the number of accessible states to the radiation is not $O(N^2)$ and we will have $O(1)$ degrees of freedom which leads to the small rate of the Hawking radiation. Their idea is that this reduction in the degrees of freedom is related to the curvature, so the presence of the small amount of curvature leads to make most of the CFT degrees of freedom inactive. It is also mentioned that the possibility of the non-existence of static localized large black hole is not removed by this reasoning, it can only illustrate what is not justified in the reasoning.

2.3 Numerical Attempts for Finding a Black Hole in RSII

In [62], Wiseman developed a numerical method, called the elliptic relaxation method, to study the behavior of relativistic stars in the RSII model. The method was applied to solve the Einstein equation for the RSII static metric, which was parameterized with three free functions. Assuming that the metric is axis-symmetric, solving the Einstein equation yields the elliptical partial differential equation that can be solved numerically with proper asymptotical boundary conditions. Kudoh et al. [40, 41] try to construct the

black hole solution in RSII, based on the method used in [62]. The small
localized black hole solution was found numerically. The horizon size of this
black hole was smaller than $0.2l$, where l is the bulk curvature scale. But, the
code failed to work for large horizon radius because of a lack of convergence.
This result can be seen as evidence for the existence of a small localized black
hole in RSII but not for a large one.

Yoshino [63] tried to modify the coordinates to make a more accurate code
with a fourth-order accuracy in differentiation on the bulk while the accuracy
in [40, 41] has the second-order accuracy in differentiation. The numerical
result in [63] shows that there is a nonsystematic error for the case with non-
zero tension on the brane. According to the result, Yoshino claimed that even
small localized black holes do not exist in RSII for this set-up.

Despite all the mentioned conjectures basis on either the non-existence of
black holes in RSII or the existance of the small black holes, Figueras, Luci-
etti, and Wiseman (FLW) [16] constructed a black hole solution by solving
the elliptic Ricci-DeTurck flow equation numerically. The metric has a static
black hole solution on the AdS boundary, which is conformal to the four-
dimensional Schwarzschild metric. The numerical technique for the Ricci-
DeTruck equation and flow to solve the Einstein equation was discussed in
[30]. Afterwards, Figueras and Wiseman [17] perturbed the numerical results
for the AdS_5-CFT_4 solution found in [16]. The perturbation gives an RSII so-
lution with a large brane-localized black hole. This result was the first report
on finding the large black hole solution in RSII successfully.

Meanwhile, the same problem has been probed by our group, including S.
Abdolrahimi, C. Cattoën, D. N. Page, and Shime Yaghoobpour Tari [1, 2].

We have found the same result that confirms the existence of a large black hole in RSII. We have used a different and independent method to find an AdS_5-CFT_4 solution by solving the Einstein equation. Then, we have perturbed our solution in the same way as FW to find the large black hole solution. In the following chapters, we present our work as the subject of this thesis.

In Chapter 3, we will describe the spectral method that we have used to find the numerical solution for the Einstein equation with the negative cosmological constant. We will go through all the numerical results and plots for the metric and its energy-momentum components. C. Cattoën has written the numerical code in MATLAB for finding the solution for Einstein equation. Shima Yaghoobpour Tari has worked with the code, written the required files in Maple, and tranferred them to MATLAB code to get the numerical results and plots, as well as the final check for the values for the integrals in Maple to confirm the MATLAB result. The energy-momentum tensor components has been calculated in Maple by Shima Yaghoobpour Tari, using the numerical result.

In Chapter 4, the perturbed metric, which is the large black hole metric in RSII spacetime, will be derived. The mass, temperature, entropy and area for the RSII black hole metric will be compared with the Schwarzschild metric up to the first-order of the perturbation parameter.

A comparison between the FLW result and our result has been made for different components of the energy-momentum tensors in Chapter 5. It can be seen that the numerical results are in close agreement, which can confirm the existence of the large black hole in RSII. The comparison is made by finding the fitting functions for FLW results and ours. Shima Yaghoobpour

Tari has done the numerical calculations for finding the fitting functions in Maple, which S. Abdolrahimi has also done in parallel as a check.

In chapter 6, we will try to wrap up all the results and make a conclusion regarding what we have done.

Chapter 3

Infinite-Mass Black Hole in the RS II Braneworld Model

Our work is focusing on finding a large static black hole in the RSII model. First, we start by constructing a five-dimensional numerical solution for the Einstein equation with a negative cosmological constant, Λ. The metric is an AdS_5-CFT_4 solution, asymptotically conformal to the Schwarzschild metric, where the Schwarzschild metric is located at the AdS_5 boundary with an infinite scale factor, so it can be considered as a black hole with an infinite mass. We derive the energy-momentum tensors numerically for the infinite-mass metric to use them for the next step, which is the perturbation of the infinite-mass black hole metric, and check the energy-momentum conservation.

In this chapter, we will go through all the steps, numerical methods, and results that we have done in our work.

3.1 Method Description for Finding the Infinite-Mass Black Hole

3.1.1 Setup for a Trial Metric

We try to set up a trial black hole metric on the basis of the RSII metric by adding some smooth functions to remove the problem we ran into for the first proposed black string metric based on the RSII model [8]. Then, we will solve the Einstein equation for this trial metric. We start with the AdS metric (2.2), with h_{ab} defined as the Schwarzschild metric. So, we try to make our metric by looking at the black string metric,

$$ds^2 = \frac{l^2}{z^2}\left[-U(r)dt^2 + U(r)^{-1}dr^2 + r^2(d\Omega^2) + dz^2\right],　\quad (3.1)$$

where $U(r) = 1 - \frac{2M}{r}$ and $d\Omega^2 = d\theta^2 + \sin^2\theta d\phi^2$ is the unit two-sphere metric. Applying the transformation $y = \frac{2M}{r}$, $z = \frac{2M}{v}$ and choosing units so that $l = 1$, the black string metric becomes

$$ds^2 = \frac{dv^2}{v^2} + \frac{v^2 dy^2}{y^4(1-y)} - 4v^2(1-y)dt^2 + \frac{v^2}{y^2}d\Omega^2, \quad (3.2)$$

with $0 \leq y \leq 1$, where $y = 1$ is the black hole horizon, and $0 \leq v \leq \infty$, where $v = 0$ is the AdS horizon. As mentioned before, the metric is singular at $v = 0$, since the curvature diverges for $y > 0$ at $v = 0$. We replace this singularity by a regular axis, where we add y^2 terms to the metric. And, we parameterize the resulting metric by four free functions. Then the infinite

black hole metric is

$$ds^2 = A\frac{dv^2}{y^2 + v^2} + B\frac{(y^2 + v^2)dy^2}{y^4(1 - y)} - 4C(y^2 + v^2)(1 - y)dt^2 + D\frac{v^2}{y^2}d\Omega^2. \qquad (3.3)$$

Applying another transformation, $x = \frac{y^2}{y^2 + v^2}$, gives

$$ds^2 = A(1 - x)\left[\frac{dx}{2x(1 - x)} - \frac{dy}{y}\right]^2 + B\frac{dy^2}{xy^2(1 - y)} - 4C\frac{y^2(1 - y)}{x}dt^2 + D\frac{1 - x}{x}d\Omega^2,$$

$$(3.4)$$

where $0 \leq x \leq 1$, $0 \leq y \leq 1$ and A, B, C, and D are smooth functions of x and y that all approach unity for $x = 0$.

The coordinate boundaries are these: $x = 0$ is the infinite AdS boundary that is conformal to the Schwarzschild metric, $x = 1$ is the center, the axis of symmetry where the two-sphere shrinks to zero, $y = 0$ is the extremal Poincare horizon, and $y = 1$ is the black hole horizon. The metric (3.4) is the one that we are going to work on in order to find the functional form of $A(x, y)$, $B(x, y)$, $C(x, y)$, and $D(x, y)$ as polynomials in x and y.

The most general metric satisfying all the symmetries for our problem has five components. On the other hand since the metric functions depend non-trivially on the two coordinates, x and y, and the choice of these is gauge dependent, one can reduce the number of the metric components to three. The common method for finding a unique solution for the Einstein equation numerically is to fix the gauge before discretization. Otherwise, one will have a family of solutions parametrized by one function that is gauge dependent. But in our case, we assume four unknown functions instead of three as mentioned, and we will get a unique solution. Our explanation for this result can be related to our restriction of $A(x, y)$, $B(x, y)$, $C(x, y)$, and $D(x, y)$ to poly-

nomials for simplicity; we also tried rational functions, but they did not seem
to work numerically so well, as shall be mentioned later. Having polynomials
of some fixed finite order means that with such restricted functions, some
gauges are better than others. For clarification, we can consider the case of a
spherically symmetric static metric

$$ds^2 = -A(x)dt^2 + \frac{1}{B(x)}dx^2 + \frac{1}{C(x)}d\Omega^2. \tag{3.5}$$

If we consider the restriction for $A(x,y)$, $B(x,y)$, and $C(x,y)$ to be poly-
nomials, then with having all three functions, one can find $A(x) = 1 - x$,
$B(x) = x^4 - x^5$, and $C(x) = x^2$ solves the vacuum Einstein equations. How-
ever, if one choose the gauge $B(x) = 1$, no polynomials of finite order would
give an exact solution, and we would expect greater error. On the other hand,
we are not looking for an exact solution, so with our restriction to have a fixed
order of polynomials for each function, surely we would get a better result
with more functions, even if for an exact solution one or more functions would
be just gauge.

At the boundaries, for $x = 0$, the metric has to be conformally Schwarzschild,
so we impose $A = B = C = D = 1$ there; for $x = 1$, at the center, we impose
$A = D$ for regularity; and for $y = 1$, the black hole horizon, we impose $B = C$
since the surface gravity should be constant and positive at the horizon. Ap-
plying these conditions, solving the Einstein equation to the lowest order in
x, and considering that our solution has to be regular everywhere between
the horizons leads us to the preliminary functional form of $A(x,y)$, $B(x,y)$,

$C(x, y)$, and $D(x, y)$ as

$$
\begin{align}
A(x, y) &= 1 - x(1 - x)(1 + 2f(y)) + x^2 g(y) + x^2(1 - x)PA(x, y), &\text{(3.6)} \\
B(x, y) &= 1 + xf(y) + x^2 PB(x, y), &\text{(3.7)} \\
C(x, y) &= 1 + xf(y) + x^2 PB(x, y) + x^2(1 - y)PC(x, y), &\text{(3.8)} \\
D(x, y) &= 1 + x(1 - x)(1 + f(y)) + x^2 g(y) + x^2(1 - x)PD(x, y). &\text{(3.9)}
\end{align}
$$

Now, our problem is to solve the Einstein equation numerically for the metric (3.4) in order to find the six unknown smooth functions $f(y)$, $g(y)$, $PA(x, y)$, $PB(x, y)$, $PC(x, y)$, and $PD(x, y)$, which for simplicity we took to be polynomials (or rational functions in some trial calculations that did not work so well).

3.1.2   Minimization Method for Solving the Einstein Equation

We have constructed a trial metric, which is regular at boundaries. For the next step, our goal is to find the metric as a solution that satisfies the Einstein equation for the vacuum in the five-dimensional bulk. The five-dimensional Einstein equation is

$$
R_{\alpha\beta} = \frac{2}{3}\Lambda_5 \, g_{\alpha\beta}, \qquad\qquad\qquad \text{(3.10)}
$$

where Λ_5 is the cosmological constant for the five-dimensional bulk and $R_{\alpha\beta}$ is the Ricci tensor. For an AdS model in D dimensions, Λ can be defined in

terms of a length scale l as

$$\Lambda_D = \frac{-(D-1)(D-2)}{2l^2}. \tag{3.11}$$

In our model, $\Lambda = -6/l^2$ for $D = 5$. We set $l = 1$ for the unit system that we are working in, then we define $E_{\alpha\beta}$ as

$$E_{\alpha\beta} = R_{\alpha\beta} + 4g_{\alpha\beta}. \tag{3.12}$$

Therefore, the Einstein equation in the bulk is $E_{\alpha\beta} = 0$. Now, we define an integral I, the integrated square error of the Einstein equation, as

$$I = \int E_{\alpha\beta} E^{\alpha\beta} \sqrt{-^{(5)}g} \, d^5x, \tag{3.13}$$

where $^{(5)}g$ is the metric determinant. We choose a fixed finite range for t, defined as $\Delta t = 2\pi$, to get a finite integral. The metric determinant $^{(5)}g$ is $\propto \frac{1}{x^6}$ and at $x = 0$, the infinite AdS boundary, diverges. So, we assume that $E_{\alpha\beta} E^{\alpha\beta}$ falls off fast enough to make the integral converge.

To find the metric components, we plug the functions (3.6)-(3.9) into the metric (3.4) to calculate $E_{\alpha\beta}$, the metric determinant, and finally the integral I. Then, we use a spectral method to minimize the square error that lead us to have a metric which gives a good approximation to satisfying $E_{\alpha\beta} = 0$. In the next sections, we describe the numerical method and results that we derive.

3.1.3 Numerical Method to Minimize the Squared Error of the Einstein Equation

We use a computational code, running in the MATLAB environment, to do the minimization for the squared error of the Einstein equation. The computational code is designed to do two main jobs in order to solve our required problem. The first one is the calculation of the two dimensional integral numerically, and the second one is optimization. The numerical integration method is based on Gauss-Lobatto quadrature in two dimensions, and the optimization method is an unconstrained nonlinear optimization. Their accuracies can assure us that we are numerically near an exact solution for our problem. Both methods have defined commands on MATLAB. In the following lines, we give a brief description about how these methods work and how our code works.

The quadrature rule is a numerical integration formula for the definite integral as

$$I(f) = \int_a^b f(x)dx \approx \sum_{j=0}^n w_j f(x_j), \tag{3.14}$$

where $\{x_j\}$ are called the nodes and defined on the interval $[a,b]$ and $\{w_j\}$ are weights assigned to each x_j. This formula is to be exact for polynomials of some maximum order. $f(x)$ can then be written as $W(x)g(x)$, where $W(x)$ is a defined function and $g(x)$ is a polynomial. Then,

$$I(f) = \int_a^b W(x)g(x)dx \approx \sum_{j=0}^n w_j' g(x_j). \tag{3.15}$$

Then for each such function, x_j and w'_j would be determined by means of the known orthogonal polynomials.

As an example, for the interval $[-1, 1]$, $W(x) = 1$ and $g(x)$ as a polynomial of degree j, the assigned orthogonal polynomials would be Legendre polynomials. The nodes $\{x_j\}$ are the jth root of a j-degree Legendre polynomial and w_j is

$$w_j = \frac{2}{(1 - x_j^2)[P'_n(x_i)^2]} \ . \tag{3.16}$$

Integrals on any other finite interval can be converted to the ones over $[-1, 1]$. So this example is a proper one to calculate the integral.

For the Gauss-Lobatto quadrature, both ends of the interval are counted as nodes in addition to the other nodes. This is an accurate calculation for the polynomials up to the $(2n - 1)$-degree for the $n + 1$ nodes.

The Gauss-Lobatto quadrature is the base for calculating the integral in the MATLAB algorithm that we use to evaluate our integral, which is a two dimensional integral in the two nontrivial coordinate x and y [55]. The mentioned algorithm is designed to evaluate the integral numerically over a rectangular region. The command is

$$Q = TwoD(FUN, a, b, c, d), \tag{3.17}$$

which approximates the integral

$$I(f) = \int_a^b \int_c^d f(x, y) dy dx. \tag{3.18}$$

For this program c and d can be constant or functions of x but a and b must be constants. FUN evaluates $f(x, y)$ as a vector. It takes arrays of x and y and give back the values as $Z_i = f(x_i, y_i)$ since the efficiency of the program is in the vectorization of the function $f(x, y)$. Another good point in using $TwoD$ is that it can handle a singularity on the boundary, and it is an accurate one. The default absolute error tolerance in the program is 10^{-5}, but there is an option to assign it to make it more accurate.

The optimization method is an unconstrained nonlinear optimization. The command is

$$[x, fval] = fminsearch(fun, x_0, option). \qquad (3.19)$$

The $fminsearch$ algorithm uses the Nedler-Mead simplex algorithm [44]. In this method, the program is designed to minimize a non-linear function of n variables only by means of the function value and not by any of its derivatives, which generally is called the direct simplex search method. This method can often handle discontinuity.

The algorithm works in a way that it finds the local minimum of a scalar function, fun, of several variable, starting with a set of initial values x_0, and it returns the final values x according to the local minimum and the value of the function $fval$ which is the minimum value of the function after doing the optimization. It would do it in an iterative way until it would reach the desired tolerance that is mentioned in the command or the default criteria set by the algorithm.

Now, we are going to see how our code works for our problem. We use the GRTensor package in the Maple software to make the metric (3.4) and

calculate the $E_{\alpha\beta}$ components and integrand of (3.13). Then, we transfer all our components to MATLAB for using them in our code to find our six unknown functions $f(y)$, $g(y)$, $PA(x,y)$, $PB(x,y)$, $PC(x,y)$ and $PD(x,y)$ for plugging back in (3.6)-(3.9).

To start evaluating the integral and then minimizing it, we define these functions as known polynomials with unknown coefficients. For the code, we have tried three types of the polynomials: Taylor, shifted Legendre and Pade-Legendre. The shifted-Legendre are defined as $\widetilde{P}_n(x) = P_n(2x - 1)$,

$$\widetilde{P}_n(x) = \frac{1}{n!}\frac{d^n}{dx^n}[(x^2 - x)^n],\qquad(3.20)$$

for $x\varepsilon[0,1]$. The Pade-Legendre is the division of two different orders of shifted-Legendre.

We start with the 0th of each polynomials and to get the more accurate result try the higher order polynomials step by step. The Taylor series had the slowest rate of convergence for the optimization, the Pade-Legendre was not as good as the shifted-Legendre, and finally our best choice was determined by the shifted-Legendre. So from now on we will use the shifted-Legendre to describe the code.

The functions dependent only on y are defined as

$$L(y) = \sum_{i=0}^{N} a_i \widetilde{P}_i(y).\qquad(3.21)$$

The functions dependent on x and y are defined as

$$L(x,y) = \sum_{i=0}^{N}\sum_{j=0}^{N} a_{ij}\widetilde{P}_i(x)\widetilde{P}_j(y). \qquad (3.22)$$

Here N is the highest order that we use in each run, which reduces the integral to some amount, so we need to do several runs to get down to our desired tolerence. a_i and a_{ij} are called $coeff_n$, which we want to determine by doing the optimization. As mentioned, in the optimization command (3.19), we need to give the code initial values, x_0, in order to get back the final values x. We choose the initial values for our coefficients, $coeff_{n0}$, equal to zero for the first run of each order. After doing each run, the final values will be substituted for the initial values for the next run, until the optimization terminates for reaching the tolerance defined in the code.

For shifted-Legendre the number of coefficients for the $L(y)$ is equal to $N+1$, and for $L(x,y)$ is equal to $(N+1)^2$. We need to calculate this number at each order so we consider the initial values as a vector with $2[N+1]+4[(N+1)^2]$ components. Then we need to adjust the code in order to read the initial values properly. As an example, the number of the initial values for the order one is $2 \times 2 + 4 \times 4 = 20$, where the first two components are for $f(y)$, the next two component are for $g(y)$, the next four, the fifth through the eighth, are for $PA(x,y)$, and so on.

The other thing that we adjust for each order before doing the integral and optimization is determining the terminate tolerance for x, y and the integral value. We start with 10^{-5} but at the last run we need to put it 10^{-10}. As mentioned, if the code reaches to this accuracy for any of them, the run would

be terminated, and it would give us the final values and the integral value with the plot of the integrand of the integral.

We make the functional forms of $L(y)$ and $L(x,y)$ and their derivatives on Maple and then transfer them to MATLAB. This is faster to do in advance and then plug back into the code, but sometimes it made it possible that a mistake happens. So we have a test run when we want to go to the next order.

The test run is doing the integral without the optimization. When we want to do the test run, the initial values of the new order is given in a way that we put the same final values for the last run of the previous order for the coefficients with the same terms for both orders and then the remaining initial values would be zero. With this set of the initial values the integral should have the same value for both orders. If it would happen, we can be sure that the transfer has been done properly. Each order runs up to four to five times. When we see that the integral does not change much anymore, we can go to next order.

We will give the details of all our numerical results and plots for the infinite-mass black hole metric (3.4), which is what we are looking for in the first stage of our problem.

3.2 Numerical Results for the Infinite-Mass Black Hole Metric

3.2.1 Finding the Infinite-Mass Black Hole Metric

As described in the previous section, we choose different shifted-Legendre polynomials with constant unknown coefficients as variables for $f(y)$, $g(y)$, $PA(x,y)$, $PB(x,y)$, $PC(x,y)$ and $PD(x,y)$ and vary them numerically to minimize our integrand I, (3.13), in our defined finite boundary.

Choosing $A = B = C = D = 1$ gives the value of integral as $I \approx 4038$. The integrand as a function of x and y, before any optimization, is shown in Fig.(3.1). We run the code for different orders, four to five times for each order, up to order six with 210 coefficients. For the sixth-order at the last run, the value of the integral was reduced to 0.00004238, nearly eight orders of magnitude smaller than the one without optimization. The maximum value for the squared error, $E_{\alpha\beta}E^{\alpha\beta}$, within the five-dimensional spacetime for the sixth-order is 0.000154. In Table 3.2.1, the numbers of the coefficients and the values of the integral for each order is reported. As it can be seen in Table 3.2.1, the rate of convergence is slowed down as we have used the higher-order polynomials. It was too time consuming to continue to order seven to check whether the rate of convergence is continuing to slow, but conceivably it is, because of the gauge issue discussed earlier. The plots of the integrand as a function of x and y for all orders is shown in Fig. 3.2 and Fig. 3.3, the progress that we made through each step can be seen through the plots.

The numerical form of functions $f(y)$ and $g(y)$ in the complete form and

Order	No. of Coefficients	I
0	6	69.6986
1	20	1.5656
2	42	4.779×10^{-1}
3	72	2.390×10^{-2}
4	110	2.535×10^{-3}
5	156	5.416×10^{-4}
6	210	4.238×10^{-4}

Table 3.1: The number of coefficients and the numerical result for the integral (3.13) for each order of polynomials functions used in the code
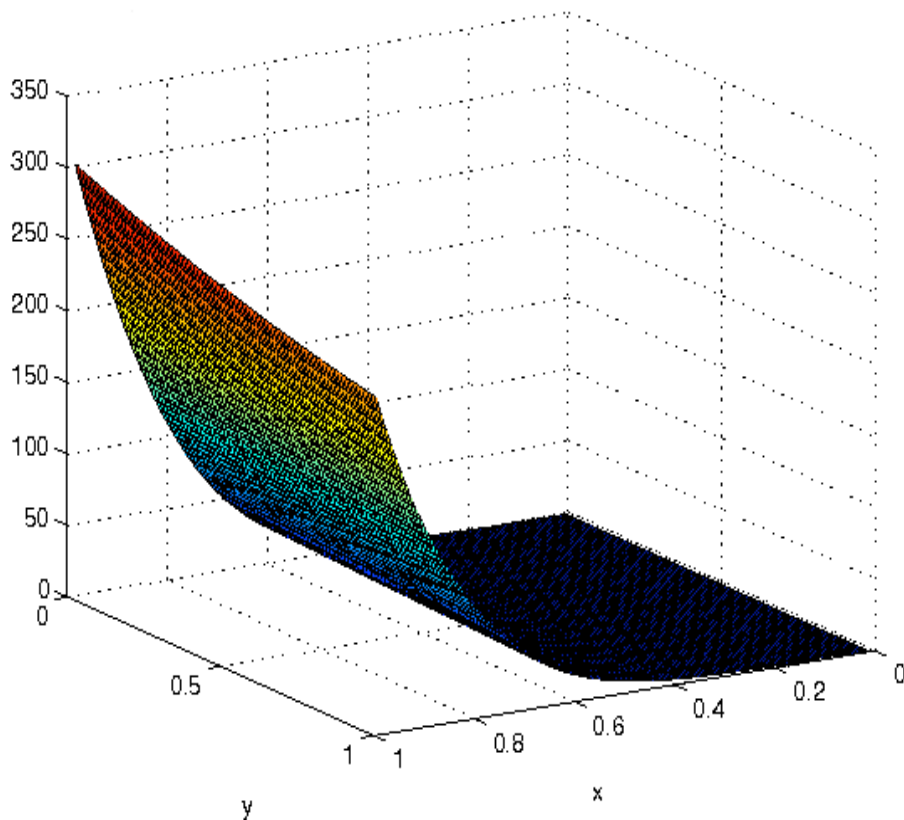
Figure 3.1: $E_{\alpha\beta}E^{\alpha\beta}$ as a function of x and y for $A = B = C = D = 1$
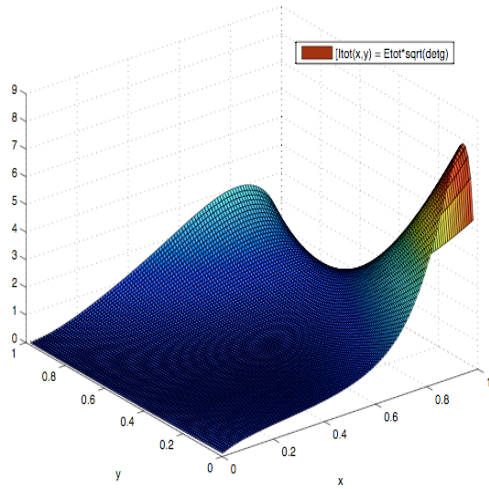
(a) 0th-Order Polynomial
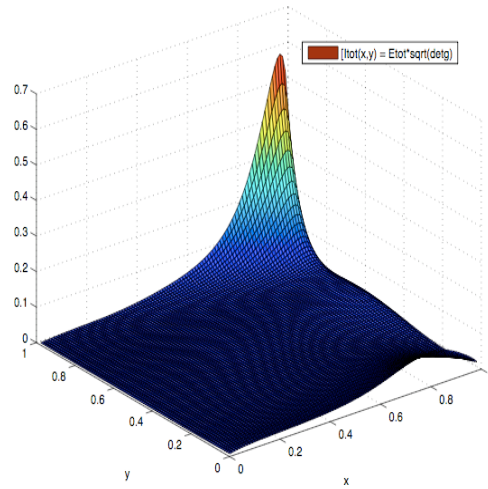
(b) 1st-Order Polynomial
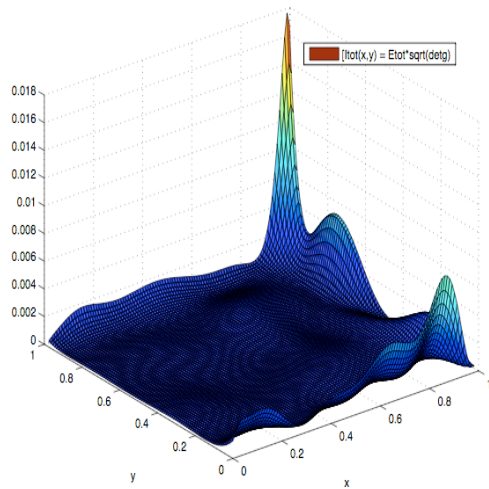
(c) 2nd-Order Polynomial
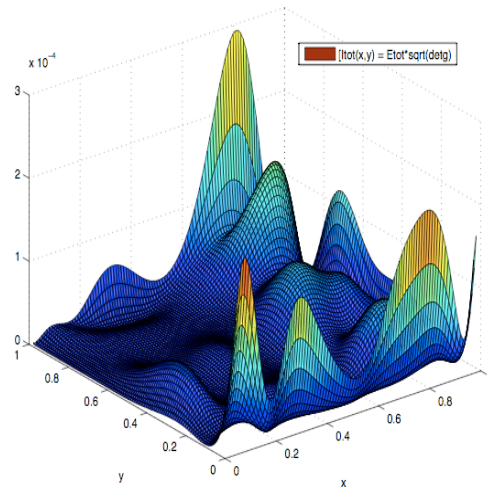
(d) 3rd-Order Polynomial

Figure 3.2: The integrand of integral (3.13) as a function of x and y for different shifted-Legendre polynomials from order-zero to order-three
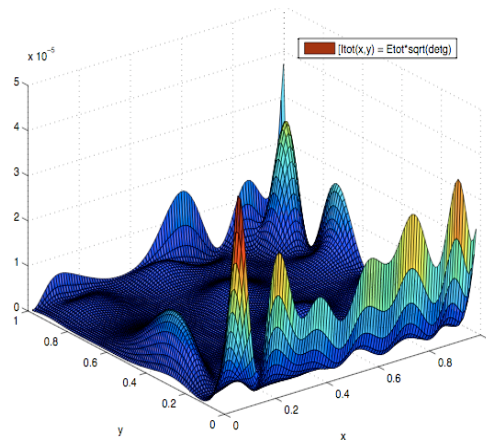
(a) 4th-Order Polynomial
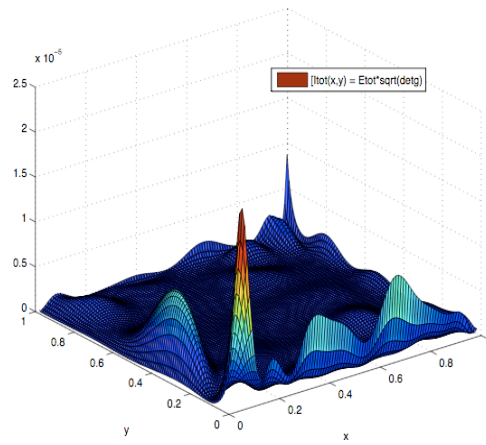
(b) 5th-Order Polynomial
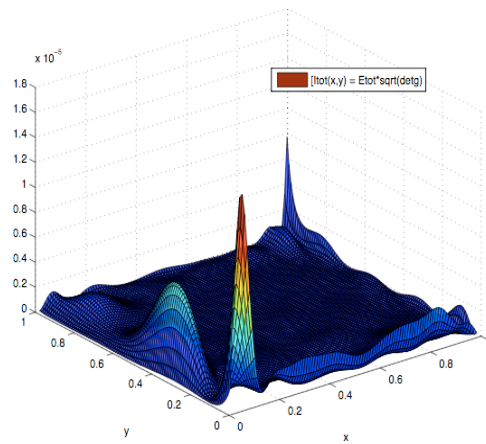
(c) 6th-Order Polynomial

Figure 3.3: The integrand of integral (3.13) as a function of x and y for different shifted-Legendre polynomials from order-three to order-six

$PA(x, y)$, $PB(x, y)$, $PC(x, y)$, and $PD(x, y)$ up to third-order in x are given as

$$
\begin{aligned}
f(y) \ = \ & -0.60547 - 0.47885y + 0.16108y^2 - 0.03931y^3 && (3.23) \\
+ \ & 0.07277y^4 - 0.04354y^5 + 0.00354y^6, && (3.24) \\
g(y) \ = \ & 0.60118 - 0.37010y + 0.19724y^2 + 0.16101y^3 \\
+ \ & 0.002320y^4 - 0.04978y^5 + 0.00066y^6, \\
PA(x, y) \ = \ & 0.09288 - 1.63742y + 2.60281y^2 + 1.50520y^3 && (3.25) \\
- \ & 3.41379y^4 + 1.55702y^5 - 0.16769y^6 + (-1.6177 + 14.32732y \\
- \ & 27.60537y^2 + 15.18000y^3 + 4.10989y^4 - 4.89926y^5 + 0.37898y^6)x \\
+ \ & (4.16674 - 47.08375y + 143.17413y^2 - 199.37753y^3 \\
+ \ & 157.81384y^4 - 78.71069y^5 + 20.52872y^6)x^2 + O(x^3), \\
PB(x, y) \ = \ & 0.43149 - 0.80874y + 0.89419y^2 - 0.31160y^3 && (3.26) \\
- \ & 0.09758y^4 + 0.08441y^5 - 0.00483y^6 + (0.21851 + 0.08687y \\
- \ & 1.72664y^2 + 2.47145y^3 - 0.92513y^4 - 0.07910y^5 + 0.05733y^6)x \\
+ \ & (-0.24942 + 0.72760y + 3.13465y^2 - 9.10834y^3 \\
+ \ & 8.03310y^4 - 3.11900y^5 + 0.42050y^6)x^2 + O(x^3), \\
PC(x, y) \ = \ & -0.57665 + 1.55879y - 1.01295y^2 - 0.17390y^3 && (3.27) \\
+ \ & 0.75253y^4 - 0.43954y^5 + 0.06057y^6 + (0.05855 - 3.00551y \\
+ \ & 5.52990y^2 - 3.60880y^3 - 0.34211y^4 + 2.029580y^5 - 0.97860y^6)x \\
+ \ & (-0.29591 + 4.44010y - 12.09689y^2 + 9.21164y^3 \\
+ \ & 4.86955y^4 - 13.57664y^5 + 6.75727y^6)x^2 + O(x^3),
\end{aligned}
$$

(a) $A(x, y)$

(b) $B(x, y)$

(c) $C(x, y)$
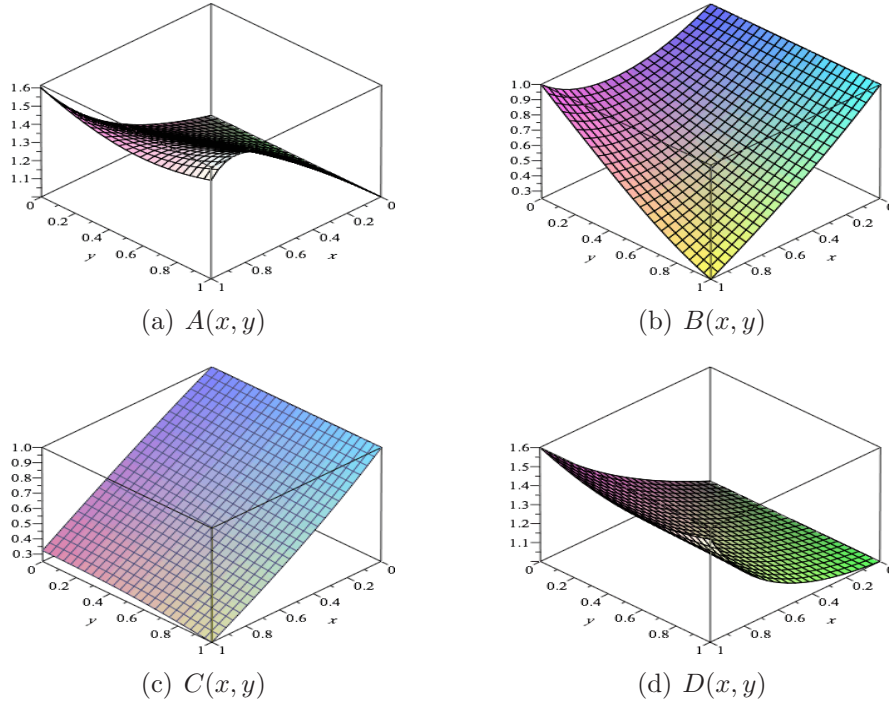
(d) $D(x, y)$

Figure 3.4: $A(x, y)$, $B(x, y)$, $C(x, y)$, and $D(x, y)$ as functions of x and y

$$
\begin{aligned}
PD(x, y) ={} & -0.15534 + 0.49821y - 0.20727y^2 - 1.30841y^3 && (3.28) \\
& + \ 1.09944y^4 - 0.23064y^5 - 0.02496y^6 + (+0.16801 - 2.00146y \\
& + \ 5.16551y^2 - 7.46325y^3 + 8.91066y^4 - 7.66198y^5 + 2.77780y^6)x \\
& + \ (-0.35730 + 5.18626y - 26.07180y^2 + 71.93564y^3 \\
& - \ 110.66600y^4 + 86.74014y^5 - 27.03106y^6)x^2 + O(x^3).
\end{aligned}
$$

The cofficients were rounded to five digits.

Plugging back the functions (3.23)-(3.28) into the equations (3.6)-(3.9) gives the numerical form of functions $A(x, y)$, $B(x, y)$, $C(x, y)$, and $D(x, y)$. The numerical result for these functions can be found in Appendix A.

Figure (3.4) shows the plots for functions $A(x, y)$, $B(x, y)$, $C(x, y)$, and $D(x, y)$ as functions of x and y. Having the functional form of $A(x, y)$, $B(x, y)$,

(a) $g_{xx}(x, y)$ (b) $g_{xy}(x, y)$ (c) $g_{yy}(y, y)$

(d) $g_{tt}(x, y)$ (e) $g_{\theta\theta}$
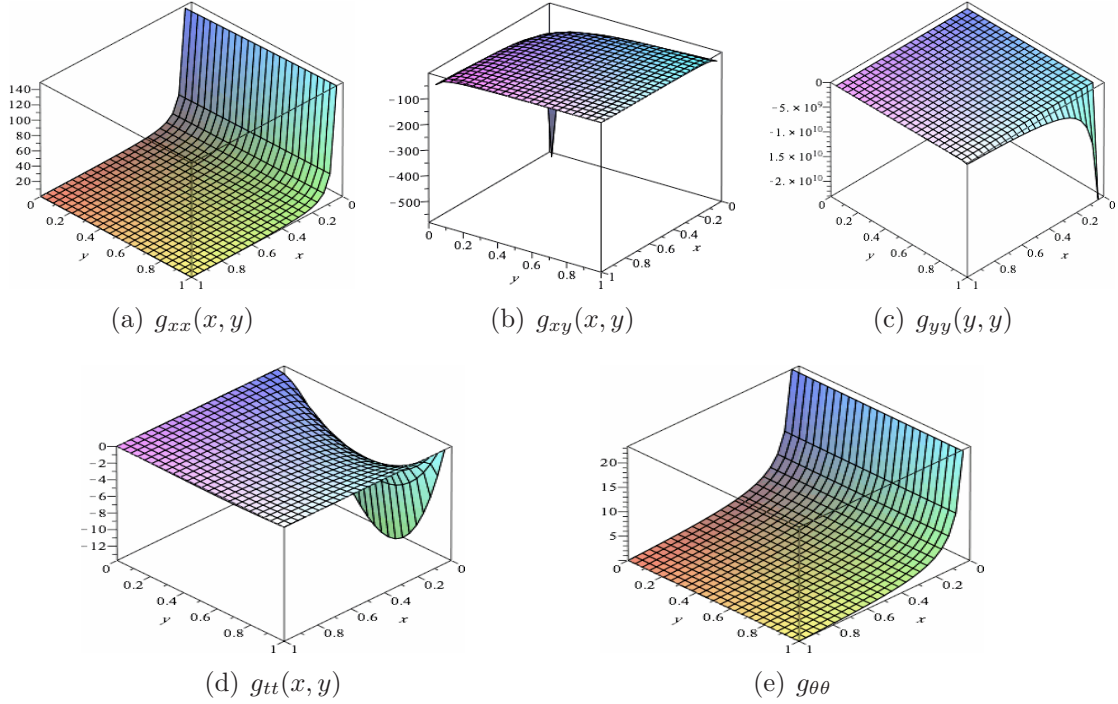
Figure 3.5: The components of metric (3.4) as functions of x and y

$C(x, y)$, and $D(x, y)$ gives us the components of metric (3.4), and this is our solution for the first part of our problem. In Figure (3.5), the plots for the metric components as functions of x and y are shown. So, we have the numeric metric for the infinite-mass black hole.

Having the numerical form of the metric helps us to analyze some features of the metric through the plots for different quantities. At black hole horizon, $y = 1$, the metric for $t = $ const. slices can be written as

$$ds^2 = A(x)\frac{1}{4x^2(1-x)}dx^2 + D(x)\frac{1-x}{x}d\Omega^2, \tag{3.29}$$

with

$$
\begin{aligned}
A(x) \quad = \quad & 1 + 0.85959x + 0.221970x^2 - 0.66519x^3 + 0.63763x^4 \qquad (3.30) \\
& - \quad 0.97718x^5 + 1.53365x^6 - 0.96168x^7 - 0.29554x^8 + 0.18927x^9, \\
D(x) \quad = \quad & 1 + 0.07021x + 0.14336x^2 + 0.22442x^3 - 0.15951x^4 \qquad (3.31) \\
& + \quad 0.54809x^5 - 0.71742x^6 + 0.60302x^7 - 0.19459x^8 + 0.02494x^9.
\end{aligned}
$$

For the metric (3.29), the squared Ricci tensor, $R_{\mu\nu}R^{\mu\nu}$, and Ricci scalar, R, as functions of x are calculated and plotted in Fig. 3.2.1. We can see that both of them are finite through the interval $x \, \epsilon [0, 1]$. The squared Ricci tensor is 12 at $x = 0$ (the infinite AdS boundary) and 48.49 at $x = 1$ (the axis of symmetry), and the values for the Ricci scalar are -6 at $x = 0$ and 11.75 at $x = 1$.
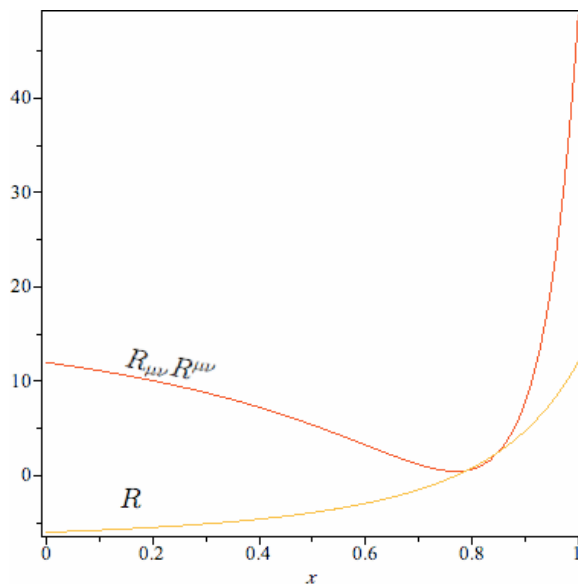
Figure 3.6: The squared Ricci tensor, $R_{\mu\nu}R^{\mu\nu}$, and Ricci scalar, R, on the black hole horizon surface for metric (3.29) as a function of x.

In Fig. 3.7, the contour lines for the $g_{tt} =$ const. surfaces and $g_{\theta\theta} =$ const. surfaces are plotted. $g_{\theta\theta} =$ const. surfaces can be considered as different radii for sphere defined by the line element $d\Omega^2$. In Fig. 3.7.a, it can be seen that the gauge that we have chosen to work with for our metric leave $g_{\theta\theta}$ rather independent of y. In addition, we have studied the behavior of the fourth root of the Weyl tensor, $(C_{\alpha\beta\gamma\delta}C^{\alpha\beta\gamma\delta})^{\frac{1}{4}}$. In Fig. 3.10, the fourth root of Weyl tensor as a function of x and y is plotted. We can see that it is zero along the AdS boundary, $x = 0$, and the extremal Poincare horizon, but it is not zero at the black hole horizon, $y = 1$, and at the center. The maximum value is at $(x, y) = (1, 1)$, which is 4.863.

(a) $g_{tt} =$ const. contour lines

(b) $g_{\theta\theta} =$ const. contour lines
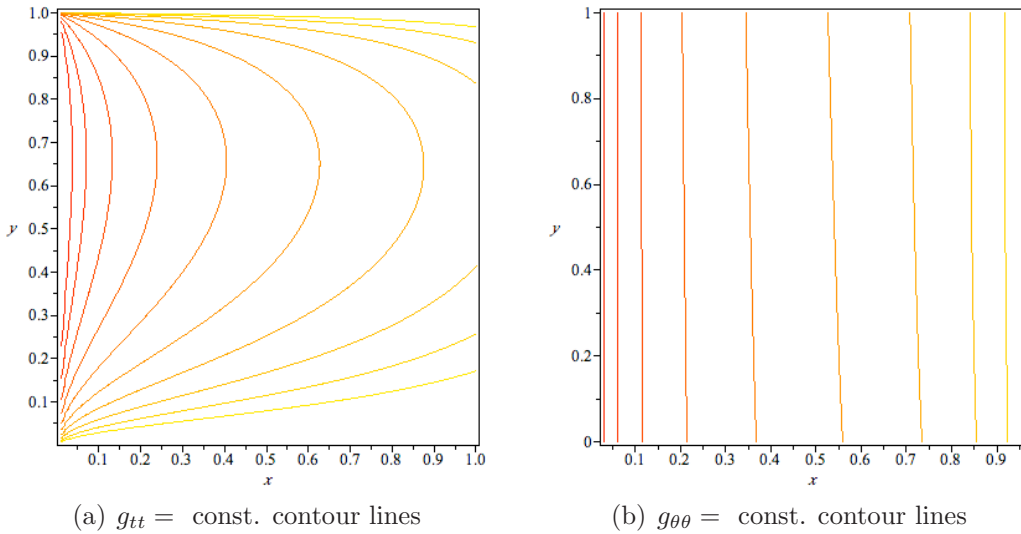
Figure 3.7: (a) The $g_{tt} =$ const. contour lines are from 16 at the leftmost to $\frac{1}{32}$ at the rightmost; each value is the half of the preceding one and (b) The $g_{\theta\theta} =$ const. contour lines are from 32 at the leftmost to $\frac{1}{16}$ at the rightmost; each value is the half of the preceding one.
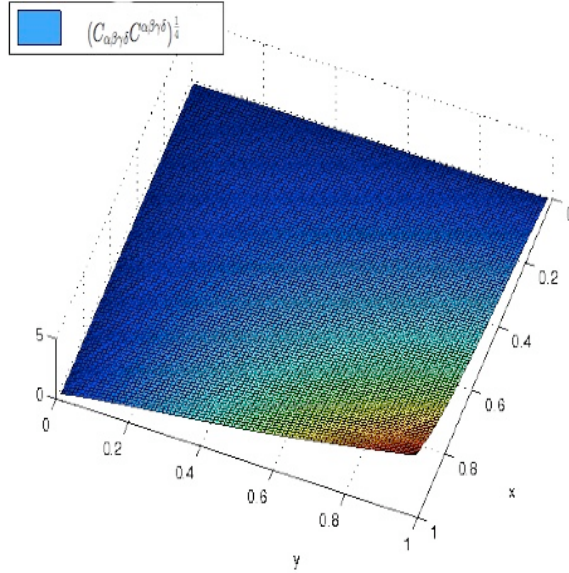
Figure 3.8: The fourth root of Weyl tensor, $(C_{\alpha\beta\gamma\delta}C^{\alpha\beta\gamma\delta})^{\frac{1}{4}}$, as a function of x and y.

3.2.2 Energy-Momentum Tensor for the Infinite-Mass Black Hole

In this section, we are trying to find and study the behavior of the energy-momentum tensor at the AdS boundary. The derived infinite-mass black hole metric is conformally Schwarzschild at the infinite AdS boundary, $x = 0$. Using this feature in the Fefferman-Graham expansion [25, 26, 29] leads us to determine the energy-momentum tensor on the boundary. It is good to mention that the energy-momentum tensor in the Fefferman-Graham expansion is a mathematical tensor that can be related to the CFT energy-momentum tensor on the boundary in the dual CFT picture, assuming that AdS/CFT can be applied for our situation. But, it is different from the non-zero bulk energy-momentum tensor as a source for the Einstein equation.

For the infinite region, the asymptotic form of the five-dimensional bulk metric near the boundary can be written as

$$ds^2 = dr^2 + e^{2r}\tilde{g}_{\mu\nu}(r,x)dx^\mu dx^\nu, \tag{3.32}$$

where $r \sim ln\ v$, which is the outward proper distance as one approaches the AdS boundary at infinite proper distance, and x is not the same coordinate used for the numerical result but instead it denotes all the other four coordinates other than r.

According to the Fefferman-Graham coordinate system, any AdS metric can be rewritten in the form (3.32) with

$$
\begin{aligned}
\tilde{g}_{\mu\nu}(r,x) =\ & g_{\mu\nu}^{(0)}(x) + e^{-2r}\left(-\frac{1}{2}R_{\mu\nu}^{(0)}(x) + \frac{1}{12}g_{\mu\nu}^{(0)}(x)R^{(0)}(x)\right) \\
& + e^{-4r}g_{\mu\nu}^{(4)}(x) - 2e^{-4r}rh_{\mu\nu}^{(4)}(x) + e^{-4r}t_{\mu\nu}(x) + O(e^{-6r}).
\end{aligned}
\tag{3.33}
$$

$g_{\mu\nu}^{(0)}(x)$ is a asymptotic conformal metric on AdS boundary and $R_{\mu\nu}^{(0)}(x)$ is the Ricci tensor for the $g_{\mu\nu}^{(0)}(x)$ metric. Solving the bulk Einstein equation as a second-order differential equation in the radial coordinate r for the Fefferman-Graham form determines $g_{\mu\nu}^{(0)}(x)$ as a conformal metric on the AdS boundary and the tensor $t_{\mu\nu}(x)$ as a divergenceless and traceless tensor after applying the boundary condition. The terms $g_{\mu\nu}^{(4)}(x)$ and $h_{\mu\nu}^{(4)}(x)$ are functions of the Ricci tensor $R_{\mu\nu}^{(0)}(x)$; see [15] for their exact definitions. As mentioned, we set $g_{\mu\nu}^{(0)}(x) = g_{\mu\nu}^{\text{Sch}}$ for our metric (3.4) at the $r = \infty$ boundary. The $g_{\mu\nu}^{\text{Sch}}$ is the Schwarzschild metric, which is Ricci-flat. So, the only non-zero terms in (3.33), which is an expansion up to order $O(e^{-6r})$, are the terms including

$g_{\mu\nu}^{(0)}(x)$ and $t_{\mu\nu}(x)$. The metric has the asymptotic form

$$ds^2 = dr^2 + e^{2r}\left[e^\beta \frac{dy^2}{y^4(1-y)} - 4e^\gamma(1-y)dt^2 + e^\delta \frac{1}{y^2}d\Omega^2\right], \qquad (3.34)$$

$$
\begin{aligned}
\beta &= e^{-4r}\, t_r{}^r(y) + O(e^{-6r}),\\
\gamma &= e^{-4r}\, t_t{}^t(y) + O(e^{-6r}),\\
\delta &= e^{-4r}\, t_\theta{}^\theta(y) + O(e^{-6r}).
\end{aligned}
$$

$t_r{}^r$, $t_t{}^t$, and $t_\theta{}^\theta$ are the components of the traceless, divergenceless tensor $t^\mu_\nu(y)$, which is diagonal in our coordinate system. In accordance with the AdS/CFT correspondence, the gravitational field on the brane can be related to the expectation value of the energy-momentum tensor for the CFT with large N, number of the CFT fields involved, and strong coupling as

$$G_{\mu\nu} = 8\pi G_4 \langle T_{\mu\nu}^{CFT}\rangle. \qquad (3.35)$$

See [11, 47]. Having the metric in Fefferman-Graham form and using equation (3.35) can relate the $t_{\mu\nu}$ to $\langle T_{\mu\nu}^{CFT}\rangle$ as $\langle T_{\mu\nu}^{CFT}\rangle = t_{\mu\nu}/(4\pi l G_5)$ [17].

Comparing our numerical metric with the metric form (3.33) results in finding $t_{\mu\nu}$ as a function of y. We apply the coordinate transformation for x and y with $v = y(\frac{1-x}{x})^{\frac{1}{2}} \sim e^r$ to find the asymptotic form of the infinite black hole at large v to compare with the Fefferman-Graham form. At our boundary for $x \sim \frac{y^2}{v^2}$, we find the energy-momentum tensors as functions of y, by using the coefficients of the first and second orders of x in $A(x,y)$, $B(x,y)$, $C(x,y)$, and $D(x,y)$, which are functions of y. We call them $A1(y)$, $B1(y)$,

$C1(y)$, and $D1(y)$ for the coefficient of x and $A2(y)$, $B2(y)$, $C2(y)$, and $D2(y)$ for the coefficient of x^2. Then, we calculate $t_r{}^r$, $t_t{}^t$, and $t_\theta{}^\theta$ by using these functions with the following formulas:

$$
\begin{aligned}
t_r{}^r(y) &= -\frac{1}{16}y^4\left[11 - 14y - (10 - 14y - 3A1)A1 - 4A2\right. \tag{3.36}\\
&\quad - \left. 16B2 - (12y - 13y^2)\frac{dA1}{dy} - 2(y^2 - y^3)\frac{d^2A1}{dy^2}\right], \\
t_t{}^t(y) &= -\frac{1}{16}y^4\left[-1 - 2y + 2(1 + y + 3A1)A1\right. \tag{3.37}\\
&\quad - \left. 4A2 - 16C2 + y^2\frac{dA1}{dy}\right], \\
t_\theta{}^\theta(y) &= \frac{1}{16}y^4\left[5 - 4y - (6 - 4y + 3A1)A1\right. \tag{3.38}\\
&\quad + \left. 4A2 - 16D1 + 16D2 - 2(y - y^2)\frac{dA1}{dy}\right].
\end{aligned}
$$

Plugging back the functions $A1(y)$, $B1(y)$, $C1(y)$, and $D1(y)$ and $A2(y)$, $B2(y)$, $C2(y)$, and $D2(y)$ from our numerical results to the equations for $t_r{}^r$, $t_t{}^t$, and $t_\theta{}^\theta$, (3.36)-(3.38), gives us

$$
\begin{aligned}
t_r{}^r(y) &= -0.01174y^4 + 0.38148y^5 - 0.85298y^6 + 1.36570y^7 - 2.01560y^8 \\
&\quad + 1.91160y^9 - 0.80470y^{10} + 0.08460y^{11} - 0.00739y^{12} + 0.00496y^{13} \\
&\quad - 0.00181y^{14} + 0.00023y^{15} - 0.00001y^{16}, \tag{3.39} \\
t_t{}^t(y) &= 0.00341y^4 + 0.48856y^5 - 1.18280y^6 + 1.10450y^7 - 0.03021y^8 \\
&\quad - 0.65406y^9 + 0.36864y^{10} - 0.03968y^{11} - 0.00739y^{12} + 0.00496y^{13} \\
&\quad - 0.00181y^{14} + 0.00023y^{15} - 0.00001y^{16}, \tag{3.40}
\end{aligned}
$$

$$\begin{aligned}
t_\theta{}^\theta(y) \quad = \quad & 0.00261y^4 - 0.40736y^5 + 0.86236y^6 - 0.78244y^7 + 0.28004y^8 \\
+ \quad & 0.02035y^9 - 0.03666y^{10} + 0.01027y^{11} - 0.00739ey^{12} + 0.00496y^{13} \\
- \quad & 0.00181y^{14} + 0.00023y^{15} - 0.00001y^{16}.
\end{aligned} \tag{3.41}$$
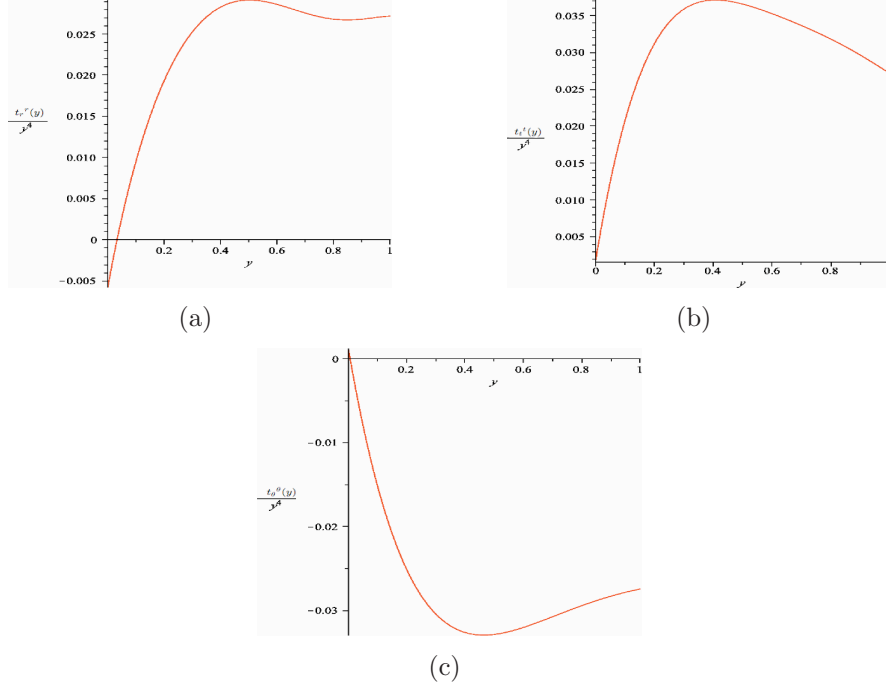
Figure 3.9: The energy-momentum tensor components as functions of y. The vertical axis corresponds to the energy-momentum components divided by y^4. (a) $\frac{t_r{}^r(y)}{y^4}$ vs. y (b) $\frac{t_t{}^t(y)}{y^4}$ vs. y (c) $\frac{t_\theta{}^\theta(y)}{y^4}$ vs. y

It can be shown that the energy-momentum tensors $t_{\mu\nu}(y)$ behave as y^5 asymptotically [16, 17]. Our numerical functions of $t_{\mu\nu}$ tensors are polynomials that start from y^4, which can be related to the numerical error since the coefficient of this term is small for all components. Fig. 3.9 show the plots of $\frac{t_r{}^r(y)}{y^4}$, $\frac{t_t{}^t(y)}{y^4}$, and $\frac{t_\theta{}^\theta(y)}{y^4}$ versus y.

The constraints on $t_r{}^r$, $t_t{}^t$, and $t_\theta{}^\theta$ as the energy-momentum constraints

can be derived as

$$t_r{}^r + t_t{}^t + 2t_\theta{}^\theta = 0, \tag{3.42}$$

$$2y(1-y)\frac{d}{dy}(t_r{}^r) + y(t_t{}^t - t_r{}^r) + 4(1-y)(t_\theta{}^\theta - t_r{}^r) = 0. \tag{3.43}$$

Equation (3.42) is the traceless condition for the energy-momentum tensor, $t_\mu^\mu = 0$, and equation (3.43) corresponds to $t_{;\mu}^{\mu r} = 0$. Checking our numerical result for the energy-momentum conditions, (3.42) and (3.43), shows small deviations from zero, which can be explained as the numerical error. In Fig. 3.10, the t_μ^μ and $t_{;\mu}^{\mu r}$ are plotted for different y in $[0, 1]$ interval. For traceless condition, the maximum deviation is 4.57×10^{-4} and for the $t_{;\mu}^{\mu r} = 0$ condition, it is 1.82×10^{-3}.
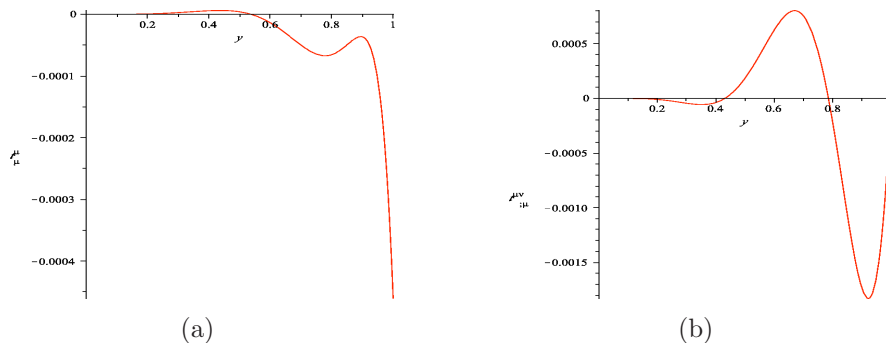
Figure 3.10: The behaviour of the energy-momentum tensor constraints for different y from 0 to 1 to see the deviation of the numerical result from 0 (a) t_μ^μ vs. y (b) $t_{;\mu}^{\mu r}$ vs. y

We have the infinite-mass black hole metric numerically. Now, we are ready to do the perturbation on this metric in order to find the finite-mass black hole on the brane in RSII, which will be the subject of the next chapter.

Chapter 4

Large Black Hole in the RS II Braneworld Model

Finding the numerical metric with an infinite mass black hole leads us to the next step, where we perturb our metric to find a large static black hole with a finite mass. Our derived metric in the last chapter is conformally Schwarzschild with infinite mass at the infinite AdS boundary, $x = 0$. We perturb the metric by replacing the infinite AdS boundary with an RSII brane with induced metric, $\gamma_{\mu\nu}$. We apply the Israel junction condition to be satisfied on the brane in order to find the perturbed metric.

In this chapter we will go through all calculations for finding the perturbed metric and study the perturbed metric to see how the mass, area, entropy and temperature of our metric is different from the Schwarzschild metric.

4.1 The Finite-Mass Black Hole

4.1.1 The Perturbed Metric

Derived from last chapter, the infinite-mass black hole, defined by the metric (3.33), has the RSII brane at $r = \infty$, AdS boundary. The metric, recalled from the previous chapter, is

$$
\begin{aligned}
\tilde{g}_{\mu\nu}(r,x) &= g^{(0)}_{\mu\nu}(x) + e^{-2r}(-\frac{1}{2}R^{(0)}_{\mu\nu}(x) + \frac{1}{12}g^{(0)}_{\mu\nu}(x)R^{(0)}(x)) \qquad (4.1) \\
&+ e^{-4r}g^{(4)}_{\mu\nu}(x) - 2e^{-4r}rh^{(4)}_{\mu\nu}(x) + e^{-4r}t_{\mu\nu}(x) + O(e^{-6r}),
\end{aligned}
$$

with $g^{(0)}_{\mu\nu}(x) = g^{\text{Sch}}_{\mu\nu}$ as the conformal Schwarzschild metric. We need to perturb the metric to find the finite mass black hole. In order to do that, we replace the RSII brane at $r = \infty$ with an RSII brane at finite proper distance $r = -\ln \epsilon$ for $\epsilon = e^{-r} \ll 1$. We suppose that there is no matter on the brane. Perturbations change the conformal metric $g^{(0)}_{\mu\nu}(x)$ as

$$
g^{(0)}_{\mu\nu} = g^{\text{Sch}}_{\mu\nu} + \epsilon^2 h_{\mu\nu}, \qquad (4.2)
$$

with the perturbation metric $h_{\mu\nu}$. For metric (4.2), the Ricci tensor is not zero, and the same is true for the e^{-2r} term in the Fefferman-Graham expansion. The perturbation would effect the tracelessness of $t^{\mu\nu}(x)$, but we can still use the values of $t^{\mu\nu}(x)$ from the infinite mass black hole bulk solution because it is multiplied by e^{-4r} in the Fefferman-Graham expansion, and we are working to lowest non-trivial order in ϵ^2.

The extrinsic curvature for the brane is calculated as

$$K_{\mu\nu} = -\frac{1}{2}\partial_r[e^{2r}\tilde{g}_{\mu\nu}(r,x)]. \tag{4.3}$$

The derivative is taken with respect to distance from the brane with the induced metric on the four-dimensional hypersurfaces, $\gamma_{\mu\nu}$, and the derivative is evaluated at zero distance from the brane. On the other hand, the second fundamental form is $[K_{\mu\nu}] = -2\gamma_{\mu\nu}$. We assume the Z_2 symmetry to be satisfied on the brane, so we have a mirror image on the opposite side of the brane and $K_{\mu\nu} = -\gamma_{\mu\nu}$. So, up to the first order in ϵ^2, the Israel junction condition gives

$$g^{(2)}_{\mu\nu} = -\frac{1}{2}R^{(0)}_{\mu\nu} + \frac{1}{12}R^{(0)}(x)g^{(0)}_{\mu\nu} = -2\epsilon^2 t_{\mu\nu}. \tag{4.4}$$

As mentioned, up to this order the $t^{\mu\nu}$ is considered traceless. Then, the Ricci tensor for the metric (4.2) is calculated as

$$R^{(0)}_{\mu\nu} = 4\epsilon^2 t_{\mu\nu}. \tag{4.5}$$

Using equation (4.5) with $t_{\mu\nu}(y)$ calculated from the infinite metric leads us to have the perturbed part of metric $h_{\mu\nu}$ and then the spherically symmetric static metric $g^{(0)}_{\mu\nu}$ in (4.2). The induced metric on the brane can be found as

$$\gamma_{\mu\nu} = \frac{1}{\epsilon^2}\tilde{g}_{\mu\nu} = \frac{1}{\epsilon^2}g^{\text{Sch}}_{\mu\nu} + h_{\mu\nu} + O(\epsilon^2). \tag{4.6}$$

The bulk Einstein equation plus the Israel junction condition on the brane without matter imply that the Ricci scalar for the metric on the brane is zero. So, to the first order in $\epsilon^2 = 1/R_0^2 = (3/2)/(-\Lambda M^2)$, the metric on the brane can be written as

$$^4ds^2 = (R_0^2 + 2b)\frac{dy^2}{y^4(1-y)} - (R_0^2 + 2c)4(1-y)dt^2 + (R_0^2 + 2d)\frac{1}{y^2}d\Omega^2. \quad (4.7)$$

We consider to work on a gauge where $h_t^t = 0$ for a general static spherically symmetric metric on the brane, which means that we choose the coordinate y so that on the brane $g_{tt} = -(1-y)$ after rescaling t in a way that $g_{tt} = -1$ at radial infinity, $y = 0$. Therefore, for a general metric on the brane that has zero Ricci scalar to lowest order in the metric perturbation on the brane, the $h_{\mu\nu}$ can be found as

$$h_y^y(y) = 2b(y) = -\frac{2y^2(1-y)}{3(4-3y)}\left(F + y\frac{dF}{dy}\right), \quad (4.8)$$

$$h_t^t(y) = 2c(y) = 0, \quad (4.9)$$

$$h_\theta^\theta(y) = h_\phi^\phi(y) = 2d(y) = \frac{y^2}{6}F(y), \quad (4.10)$$

where $F(y)$ is defined as

$$F(y) = \frac{2-3y}{(4-3y)^2}\int_0^y \frac{(4-3u)t_r{}^r(u)}{u^3(2-3u)^2}du. \quad (4.11)$$

According to (4.11), having $t_r{}^r(y)$ from the infinite-mass black hole leads us to find $F(y)$ and the $h_{\mu\nu}(y)$ components afterwards. So, we have the perturbed metric, which has a finite-mass black hole on the brane.

Considering the limit of gravity measurement allows us to have the length scale $l \leq 1\,mm$ [32, 46]. Assuming this, upper limit of l is $\sim 6 \times 10^{31}\, l_{Pl}$. Then, we can calculate the lower limit of five-dimensional cosmological constant as $\sim -6 \times 10^6$ ($\sim -2 \times 10^{65}$ in Planck unit). The Schwarzschild radius for a solar mass is $\sim 3 \times 10^3\, m$ ($\sim 2 \times 10^{38}$). Therefore, we have $\varepsilon \leq 3 \times 10^{-7}$, where $\epsilon^2 = l^2/R_0^2$.

We can rewrite the metric (4.7) as a function of F. We define a new radial coordinate $\rho = 2M/y$. Then up to the first order in $\epsilon^2 = (3/2)/(-\Lambda M^2)$, the metric (4.7) on the brane is written as

$$
\begin{aligned}
{}^4ds^2 &= \gamma_{\mu\nu}dx^\mu dx^\nu \\
&= \left[1 - \frac{1}{(-\Lambda\rho^2)}\frac{\rho - 2M}{\rho - 1.5M}\left(F - \rho\frac{dF}{d\rho}\right)\right]\left(1 - \frac{2M}{\rho}\right)^{-1}d\rho^2 \\
&\quad - \left(1 - \frac{2M}{\rho}\right)dt^2 + \left[\rho^2 + \frac{1}{(-\Lambda)}F\right]d\Omega^2,
\end{aligned}
\tag{4.12}
$$

where the coordinate t is rescaled by a factor $4M$, so the time component of metric $\gamma_{\mu\nu}$ is -1 as $\rho \to \infty$. In the next chapter, we will use this metric to do our calculations.

The next step is applying what we have found to our case to find the metric for the finite-mass black hole numerically. It is what we are going to describe in the next section.

4.1.2 The Numeric Form of the Finite-Mass Black Hole Metric

As mentioned in the previous chapter, it can be shown that the asymptotic behavior of $t_{\mu\nu}$ goes as y^5, and we know that $t_{\mu\nu}$ is traceless. This behavior of $t_{\mu\nu}$ implies that F approaches to unity as y goes to zero. But our numerical result behaves as y^4 asymptotically and has a small deviation from being traceless. However, we can consider the above characteristics for $t_{\mu\nu}$ and try to find the traceless conserved fits for $t_r{}^r$, $t_t{}^t$, and $t_\theta{}^\theta$. We define $\hat{t}_r{}^r$, $\hat{t}_t{}^t$, and $\hat{t}_\theta{}^\theta$ as follows:

$$\hat{t}_r{}^r(y) = \frac{y^5}{12(4-3y)}\left[6(1-y)F + y(2-3y)\frac{dF}{dy}\right], \qquad (4.13)$$

$$\hat{t}_t{}^t(y) = 3\hat{t}_r{}^r(y) - 2\hat{\epsilon}(y), \qquad (4.14)$$

$$\hat{t}_\theta{}^\theta(y) = -2\hat{t}_r{}^r(y) + \hat{\epsilon}(y), \qquad (4.15)$$

$$\hat{\epsilon}(y) = \frac{y^5}{12(4-3y)^2}\left[12(1-y^2)F - y(12 - 14y + 3y^2)\frac{dF}{dy}\right. \qquad (4.16)$$
$$\left. - y^2(1-y)(4-3y)\frac{d^2F}{dy^2}\right].$$

The new components $\hat{t}_r{}^r$, $\hat{t}_t{}^t$, and $\hat{t}_\theta{}^\theta$ are traceless, and their leading term is starting with y^5.

In order to find these refined components, we assume $F(y)$ is a polynomial with three unknown coefficients, $a1$, $a2$, and $a3$ and define a squared error function to minimize as

$$E = \frac{\int_0^1 [(\hat{t}_r{}^r - t_r{}^r)^2 + (\hat{t}_t{}^t - t_t{}^t)^2 + 2(\hat{t}_\theta{}^\theta - t_\theta{}^\theta)^2]\frac{dy}{y^8}}{\int_0^1 [(t_r{}^r)^2 + (t_t{}^t)^2 + 2(t_\theta{}^\theta)^2]\frac{dy}{y^8}}. \qquad (4.17)$$

Plugging back the $F(y)$ in equations (4.14)-(4.16) and minimizing the error (4.17) results in finding $a1$, $a2$, and $a3$. So, we have $F(y)$ as

$$F(y) = 1 - 1.002y + 0.434y^2 - 0.059y^3. \tag{4.18}$$

This gives $E = 0.00139$ for these values of $a1$, $a2$, and $a3$. Using this refined $F(y)$ leads us to find $\hat{t}_r{}^r$, $\hat{t}_t{}^t$, and $\hat{t}_\theta{}^\theta$. In Fig. 4.1, we plot the difference between the energy-momentum components derived form our numerical results and the ones derived from minimizing the error (4.17) as traceless and conserved components as functions of y. Also, we compared the same functions divided by y^5.

We can plug back the function $F(y)$ in equations (4.8)-(4.10), which give us the perturbed part of metric in (4.2), $h_{\mu\nu}$, as

$$
\begin{aligned}
h_y^y(y) &= 2b(y) &&(4.19) \\
&= -\frac{2y^2(1-y)}{(12-9y)}(-0.002 - 0.134y + 0.257y^2 - 0.059y^3), \\
h_t^t(y) &= 2c(y) = 0, &&(4.20) \\
h_\theta^\theta(y) &= h_\phi^\phi(y) = 2d(y) = \frac{y^2}{6}(1 - 1.002y + 0.434y^2 - 0.059y^3). &&(4.21)
\end{aligned}
$$

We have found the metric for the finite-mass black hole completely. For the next section, we will see how this black hole differs from the Schwarzschild black hole.
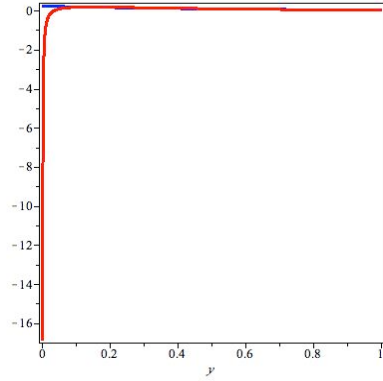
(a) $\frac{t_r{}^r(y)}{y^5}$ in red and $\frac{\hat{t}_r{}^r(y)}{y^5}$ in blue
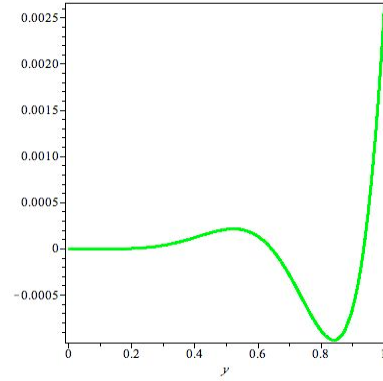
(b) $t_r{}^r(y) - \hat{t}_r{}^r(y)$
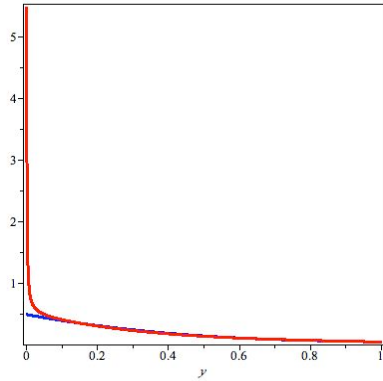
(c) $\frac{t_t{}^t(y)}{y^5}$ in red and $\frac{\hat{t}_t{}^t(y)}{y^5}$ in blue
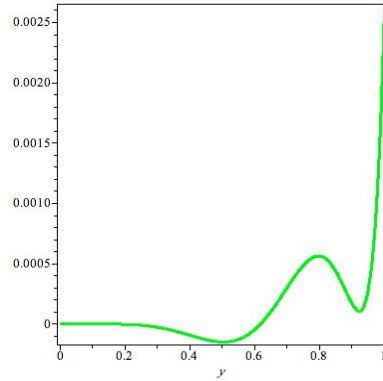
(d) $t_t{}^t(y) - \hat{t}_t{}^t(y)$
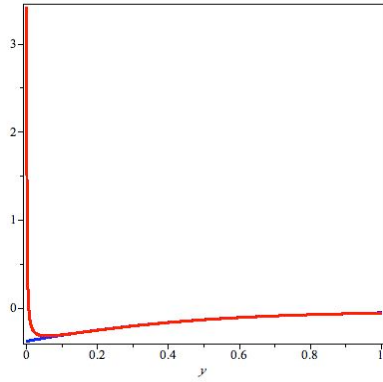
(e) $\frac{t_\theta{}^\theta(y)}{y^5}$ in red and $\frac{\hat{t}_\theta{}^\theta(y)}{y^5}$ in blue
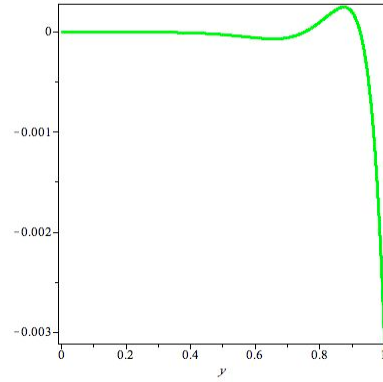
(f) $t_\theta{}^\theta(y) - \hat{t}_\theta{}^\theta(y)$

Figure 4.1: Comparing energy-momentum tensor components between the ones derived from numerical results, Eqs.(3.39)-(3.41), and the ones derived from traceless and conserved fittings, Eqs.(4.14)-(4.16) by using Eq.(4.18). The plots on the left-hand side are $\frac{t_\mu{}^\nu(y)}{y^5}$ in red and $\frac{\hat{t}_\mu{}^\nu(y)}{y^5}$ in blue, and the ones on the right-hand side are $t_\mu{}^\nu(y) - \hat{t}_\mu{}^\nu(y)$

4.2 The Mass, Temperature, Entropy and Area for the RSII Black Hole

We have found a large black hole on the brane in the RSII model by perturbing the infinite-mass black hole conformal to the Schwarzschild black hole. Now, we are going to see if there is a difference between the ADM mass, Hawking temperature, entropy and area for RSII black hole and Schwarzschild black hole.

Up to the first order in perturbation parameter, $1/(-\Lambda M^2)$, we calculate the mentioned quantities as

$$M_{RSII} \approx \frac{1}{2}R_0 + O\left(\frac{1}{\Lambda^2 M^3}\ln\left(-\Lambda M^2\right)\right), \tag{4.22}$$

$$T_{RSII} \approx \frac{1}{8\pi M} + O\left(\frac{1}{\Lambda^2 M^5}\ln\left(-\Lambda M^2\right)\right), \tag{4.23}$$

$$S_{RSII} \approx 4\pi M^2 + O\left(\frac{1}{\Lambda^2 M^2}\ln\left(-\Lambda M^2\right)\right), \tag{4.24}$$

$$A_{RSII} \approx 4\pi[R_0^2 + F(1)] + O\left(\frac{1}{\Lambda^2 M^2}\ln\left(-\Lambda M^2\right)\right) \tag{4.25}$$

$$\approx 16\pi M^2 + \frac{4\pi}{-\Lambda}F(1).$$

Here $F(1)$ is the value of the function $F(y)$ at the black hole horizon, $y = 1$. The entropy is calculated by using the surface gravity (temperature) and the mass using the first law of the black hole thermodynamics, $dM = TdS$. It can be seen that the ADM mass is exactly M with the surface gravity $1/(4M)$ and the mass-entropy relation would stay the same as the Schwarzschild to the lowest order and also the same relation for the Hawking temperature, regardless of our numerical results. On the other hand, the horizon area is

increased from the Schwarzschild one, which is $A_{Sch} = 4\pi(2M)^2$, by a term equal to $4\pi F(1)/(-\Lambda)$.

The value of $F(y)$ at the black hole horizon is 0.373. So, the difference from Schwarzschild black hole to an RSII black hole on the brane with the same ADM mass M increases the area by $\Delta A = 4\pi F(1)/(-\Lambda) \approx 4.67/(-\Lambda)$ but gives no change in the Hawking temperature and entropy. Therefore, we have shown that the large black hole on RSII brane is extremely close to what general relativity would predict. However, we should have in mind that all of these results are valid up to the first order in the expansion parameter $1/(-\Lambda M^2)$.

In the next chapter, we will try to compare our result with the FLW [16, 17] results as the first works that have been done numerically on the existence of the large black holes in the RSII model.

Chapter 5

Comparison of the First

Independent Calculations

As mentioned, Figueras, Lucietti, and Wiseman [16, 17] have found the solution for the same problem, with an independent approach. They kindly gave us their detailed numerical results to compare with ours. So, we had the chance to show that both numerical solutions are closely in agreement. In the following discussion, we will explain all calculations that we have done to do this comparison.

5.1 Comparison of the Energy-Momentum Tensor Components

As explained in the previous chapter, the perturbed part of the metric on the brane can be calculated by using the function $F(y)$, (4.8)-(4.11). Then, up to the first order in $\epsilon^2 = (3/2)/(-\Lambda M^2)$ and for the radial coordinate ρ,

$\rho \equiv 2M/y$, we have rewritten the metric on the brane as

$$
\begin{aligned}
{}^{4}ds^{2} &= \gamma_{\mu\nu}dx^{\mu}dx^{\nu} \\
&= \left[1 - \frac{1}{(-\Lambda\rho^{2})}\frac{\rho - 2M}{\rho - 1.5M}\left(F - \rho\frac{dF}{d\rho}\right)\right]\left(1 - \frac{2M}{\rho}\right)^{-1}d\rho^{2} \\
&\quad - \left(1 - \frac{2M}{\rho}\right)dt^{2} + \left[\rho^{2} + \frac{1}{(-\Lambda)}F\right]d\Omega^{2}.
\end{aligned}
\tag{5.1}
$$

It can be shown that the asymptotic behavior of $t_{\mu\nu}(x)$ at $x = 0$ and $\rho \to \infty$, $\rho \gg 2M$, should go as $1/\rho^{5}$ in order that the infinite-mass metric, (3.3), satisfy the Einstein equation. The same result has been concluded by FLW in [16, 17]. In addition, the asymptotic behavior of $t_{\mu\nu}(x)$ implies that the function F approaches unity as ρ goes to infinity. Considering the mentioned conditions for $t_{\mu\nu}(x)$ and F plus the traceless and conserved constraints for energy-momentum tensors, $t_{\mu\nu}(x)$ can be defined as functions (4.14)-(4.16) to fit with the FLW data and our data.

The numerical result for our energy-momentum tensor components, $t_{\mu\nu}^{Our}(x) = t_{\mu\nu}^{(1)}(x)$, has been derived as a function of y for $y \equiv 2M/\rho$. They have a small deviation from being traceless and conserved and also start with a y^{4} term. Therefore, we try to find a fit, $F_{1} \equiv F_{Our}$, as a cubic polynomial with the constant term set to unity and other three constant coefficients to vary. Plugging back the fit function into equations (4.14)-(4.16) gives us a traceless and conserved energy-momentum tensor, $t_{\mu\nu}^{F_{1}}(x)$. The FLW energy-momentum tensor components, $t_{\mu\nu}^{FLW}(x) = t_{\mu\nu}^{(2)}(x)$, are given as discrete points, 200 points for each component, traceless and conserved. We try to find a fit, $F_{2} \equiv F_{FLW}$ and resultant energy-momentum components, $t_{\mu\nu}^{F_{2}}(x)$. In order to find the fits,

we define the integral J_i,

$$J_i = \frac{\int \rho^4 \Delta t_{\mu\nu}^{(i)} \Delta t_{(i)}^{\mu\nu} \sqrt{-^{(4)}\gamma}\, d^4 x}{\int \rho^4 t_{\mu\nu}^{\text{FLW}} t_{\text{FLW}}^{\mu\nu} \sqrt{-^{(4)}\gamma}\, d^4 x}, \tag{5.2}$$

as the mean-square error to minimize and find the coefficients for the fitting function F_i ($i = 1$ for our data and $i = 2$ for the FLW data). $\Delta t_{\mu\nu}^{(i)} = t_{\mu\nu}^{F_i} - t_{\mu\nu}^{(i)}$ in the numerator is $t_{\mu\nu}^{F_i} - t_{\mu\nu}^{(i)}$. For increasing the weight of the large-ρ part, the factor ρ^4 is included in the numerator. However, the integrals are still dominated by the small-ρ part since $t_{\mu\nu}(x)$ drops off asymptotically as $1/\rho^5$ [16, 17]. The integral in the denominator, with the value equal to 0.00315, makes the J_i a normalized mean-square error. It is calculated by using $t_{\mu\nu}^{FLW}(x)$ from the FLW data for both J_1 and J_2. We have used the trapezoidal rule to approximate the integral as a sum with the FLW discrete data. The integral J_i can be simplified as

$$J_i = \frac{\int \rho^6 \Delta t_{\mu\nu}^{(i)} \Delta t_{(i)}^{\mu\nu}\, d\rho}{\int \rho^6 t_{\mu\nu}^{\text{FLW}} t_{\text{FLW}}^{\mu\nu}\, d\rho}. \tag{5.3}$$

For our numerical result, minimizing J_1 for $J_{Our} \approx 0.00139$ gives us $F_1 = F_{Our}$ as a function of ρ as

$$F_{\text{Our}} \approx 1 - 1.002 \left(\frac{2M}{\rho}\right) + 0.434 \left(\frac{2M}{\rho}\right)^2 - 0.059 \left(\frac{2M}{\rho}\right)^3, \tag{5.4}$$

and for the FLW data, the minimized value of the normalized mean square error is $J_{FLW} \approx 0.0000620$ for $F_2 = F_{FLW}$ as

$$F_{\text{FLW}} \approx 1 - 1.062 \left(\frac{2M}{\rho}\right) + 0.554 \left(\frac{2M}{\rho}\right)^2 - 0.120 \left(\frac{2M}{\rho}\right)^3. \tag{5.5}$$

The ratio between J_{Our} and J_{FLW} gives us $J_{Our} \approx 22 J_{FLW}$. This comes from the fact that our data is less accurate than the FLW data. For our spectral method, we have used only 210 parameters to vary for minimization, whereas FLW have used grids of 40×40 (or 1600 points) and of 160×160 (or 25600 points). In addition, the coefficients of two F_i have large relative differences, but it is not the same for the ratio of the two cubics in each point. The latter ratio never differs by more than 1.3% from unity, which shows that the fitting functions to our data and the FLW data are in a good agreement.

An 11th order polynomial fitted to the FLW data gives $J_{11} \approx 0.0000572$ for

$$
\begin{aligned}
F_{11} &= 1 - 1.1241 \left(\frac{2M}{\rho} \right) + 1.956 \left(\frac{2M}{\rho} \right)^2 - 9.961 \left(\frac{2M}{\rho} \right)^3 \\
&+ 35.475 \left(\frac{2M}{\rho} \right)^4 - 75.962 \left(\frac{2M}{\rho} \right)^5 + 99.432 \left(\frac{2M}{\rho} \right)^6 \\
&- 73.694 \left(\frac{2M}{\rho} \right)^7 + 18.726 \left(\frac{2M}{\rho} \right)^8 + 13.990 \left(\frac{2M}{\rho} \right)^9 \\
&- 12.366 \left(\frac{2M}{\rho} \right)^{10} + 2.900 \left(\frac{2M}{\rho} \right)^{11}.
\end{aligned}
\tag{5.6}
$$

This error is close to the cubic polynomial for the FLW data, 92% J_{FLW}. Therefore, F_{FLW} is good and easy enough to work with. Fig. 5.1 shows the F_{11} polynomials as a function of ρ and at the bottom, the differences between F_{Our} and F_{FLW} with F_{11} is plotted. However, it has been multiplied by 50 to make it clear since the differences are too small to show.

Table 5.1 shows the different values of J_i, using (5.3), where we have used $t_{\mu\nu}^{F_{11}}$ derived from the fitting function F_{11}, $t_{\mu\nu}^{F_{Our}}$ derived from the fitting function F_{Our}, and $t_{\mu\nu}^{F_{FLW}}$ derived from the fitting function F_{FLW}.
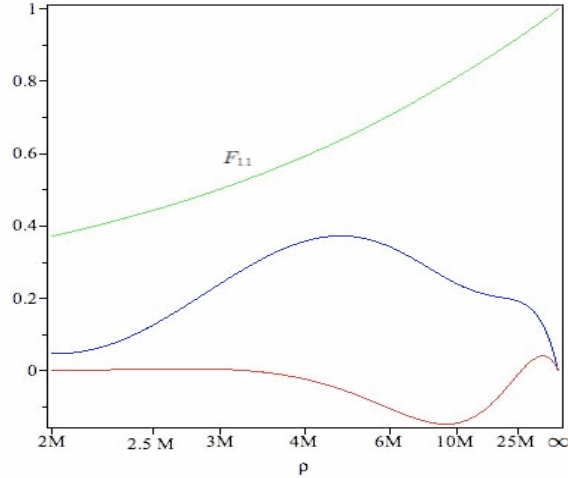
Figure 5.1: The top curve is the 11th order polynomials fitted to the FLW data. The two bottom curves are the differences between the F_{11} fit with F_{Our} and F_{FLW} fits multiplied by 50. The bottom curve is $50(F_{FLW} - F_{11})$, and the middle curve is $50(F_{Our} - F_{11})$

The integral (5.3) gives $J_{Our\ fit\ vs.\ FLW\ data} \approx 0.000214 \approx 3.4 J_{FLW}$; therefore it can be seen that $t_{\mu\nu}^{F_{Our}}$ generated by our F_{Our} fits to the FLW data much better than it fits to our data, which is about 6.5 times better. It is not unexpected, since the fit to our data was required to be traceless and conserved, where our data was not.

We also have found that $J_4 = J_{Our\ fit\ vs.\ FLW\ fit} \approx 0.000146 \approx 2.4 J_{FLW}$, which is 9 times better than the fit directly extracted from our data. It can be explained by the same reason mentioned before, which is the constraints applied to $t_{\mu\nu}^{F_{Our}}(x)$ for being traceless and conserved.

Having the fitting functions and using equations (4.14)-(4.16) give us the energy-momentum components. Each energy-momentum component for the F_{11} fit, which is the most accurate one, is plotted and the difference between this component to the same component for F_{Our} and F_{FLW} is multiplied by

	$t_{\mu\nu}^{F_{11}}$	$t_{\mu\nu}^{F_{\mathrm{FLW}}}$	$t_{\mu\nu}^{F_{\mathrm{our}}}$
$t_{\mu\nu}^{\mathrm{FLW}}$	$J_{11} \approx 0.0000572$	$J_{\mathrm{FLW}} \approx 0.0000620$	$J_3 \approx 0.000214$
$t_{\mu\nu}^{F_{\mathrm{FLW}}}$	$J_5 \approx 0.000004793$	0	$J_4 \approx 0.000146$
$t_{\mu\nu}^{F_{11}}$	0	$J_5 \approx 0.000004793$	$J_6 \approx 0.000156$

Table 5.1: Different values of J_i calculated by using Eq.(5.3), with $\Delta t_{\mu\nu}^{(i)}$ as the difference between the column $t_{\mu\nu}$ and the row $t_{\mu\nu}$.

10 and shown in Fig. 5.2.

The ratios between the values of each energy-momentum component derived from the F_{Our} to the corresponding component derived from the F_{FLW} is plotted in Fig. 5.3. The ratios between the values of each energy-momentum component derived from the fitting functions to the corresponding FLW component is plotted in Fig. 5.5. These ratios are generally within 1-2% of unity, with the maximum differing by less than 2.9%.

The trace of the square of the energy-momentum tensor, $\mathcal{T} = t_\nu^\mu t_\mu^\nu = (t_t{}^t)^2 + (t_\rho{}^\rho)^2 + 2(t_\phi{}^\phi)^2$, is plotted for the F_{11} fit in Fig. 5.4(a). The ratio between $\mathcal{T}$ for different fits and $\mathcal{T}^{\mathrm{FLW}}$, calculated directly from the FLW data, is plotted in Fig. 5.4(b). These ratios are in agreement within 3% of unity.

Comparing the energy-momentum tensor components shows a good agreement for the two independent calculations done for finding the large black hole in RSII model. For the next section, we try to compare more quantities that can be calculated or plotted.

(a)

(b)

(c)
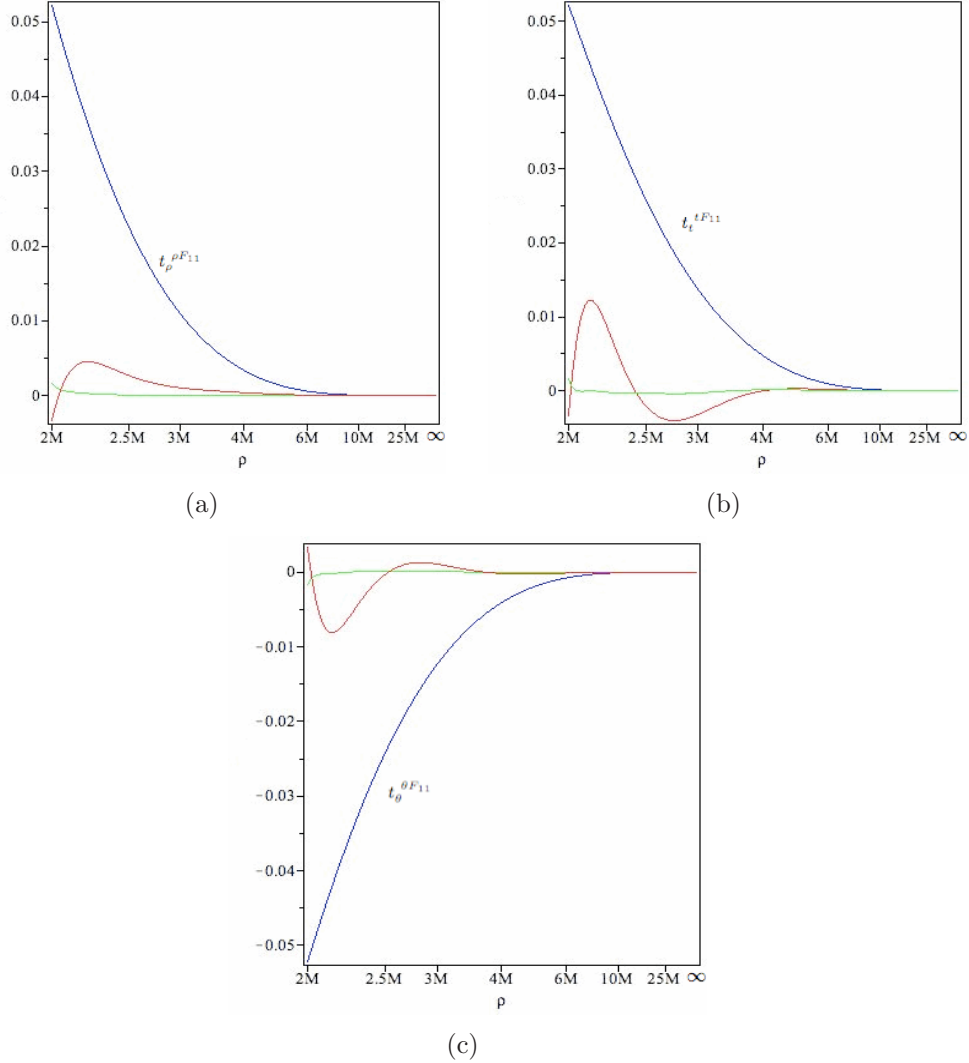
Figure 5.2: The blue curve in each graph is the energy-momentum tensor component for fitting function F_{11} as a function of ρ, and the other two curves are differences between each energy-momentum tensor component from F_{11} and the same component for F_{Our} and F_{FLW} multiplied by 10. (a) The blue curve is $t_\rho^{\rho F_{11}}$, the green one is $10(t_\rho^{\rho F_{11}} - t_\rho^{\rho F_{FLW}})$, and the red one is $10(t_\rho^{\rho F_{11}} - t_\rho^{\rho F_{Our}})$. (b) The blue curve is $t_t^{t F_{11}}$, the green one is $10(t_t^{t F_{11}} - t_t^{t F_{FLW}})$, and the red one is $10(t_t^{t F_{11}} - t_t^{t F_{Our}})$. (c) The blue curve is $t_\theta^{\theta F_{11}}$, the green one is $10(t_\theta^{\theta F_{11}} - t_\theta^{\theta F_{FLW}})$, and the red one is $10(t_\theta^{\theta F_{11}} - t_\theta^{\theta F_{Our}})$.
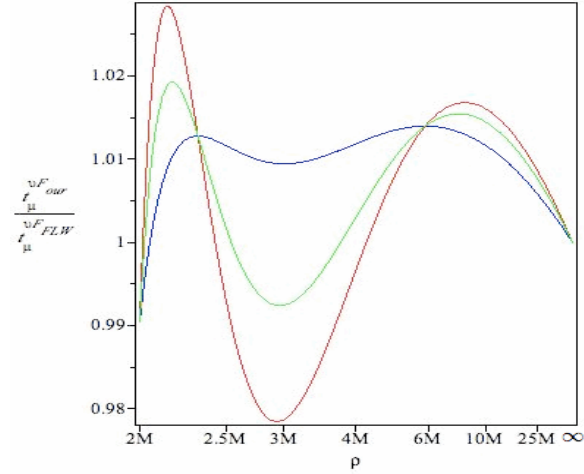
Figure 5.3: The blue, red, and green lines are the ratios of $t_\rho{}^{\rho F_{Our}}$, $t_t{}^{tF_{Our}}$, and $t_\theta{}^{\theta F_{Our}}$ to the corresponding components from F_{FLW}, respectively.

(a)

(b)
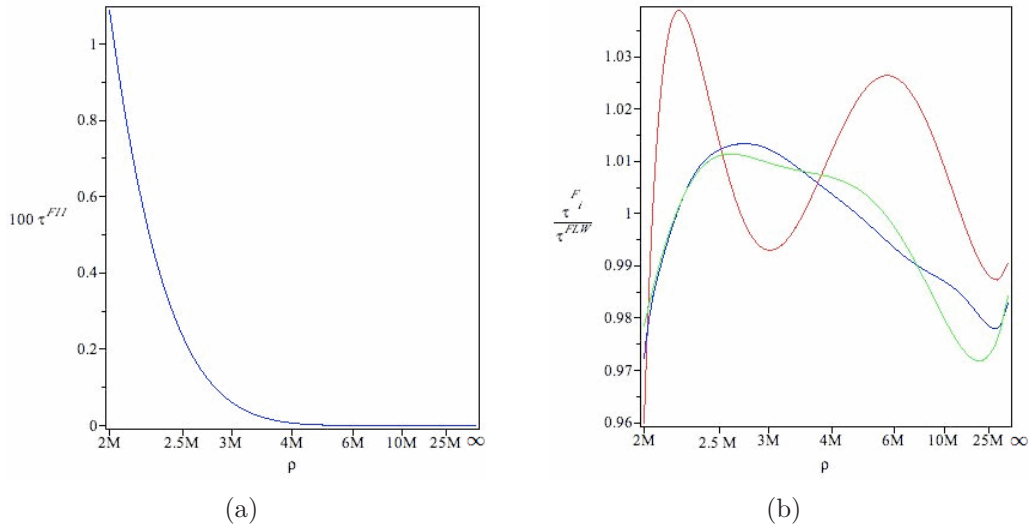
Figure 5.4: (a) Scaled $\mathcal{T}^{F_{11}} = t^{F_{11}}_{\mu\nu} t^{\mu\nu}_{F_{11}}$ vs. ρ. (b) The blue, green, and red lines are the ratios of $\mathcal{T}^{F_{11}}$, $\mathcal{T}^{F_{FLW}}$, and $\mathcal{T}^{F_{our}}$ to $\mathcal{T}^{FLW}$, respectively.

(a)

(b)

(c)
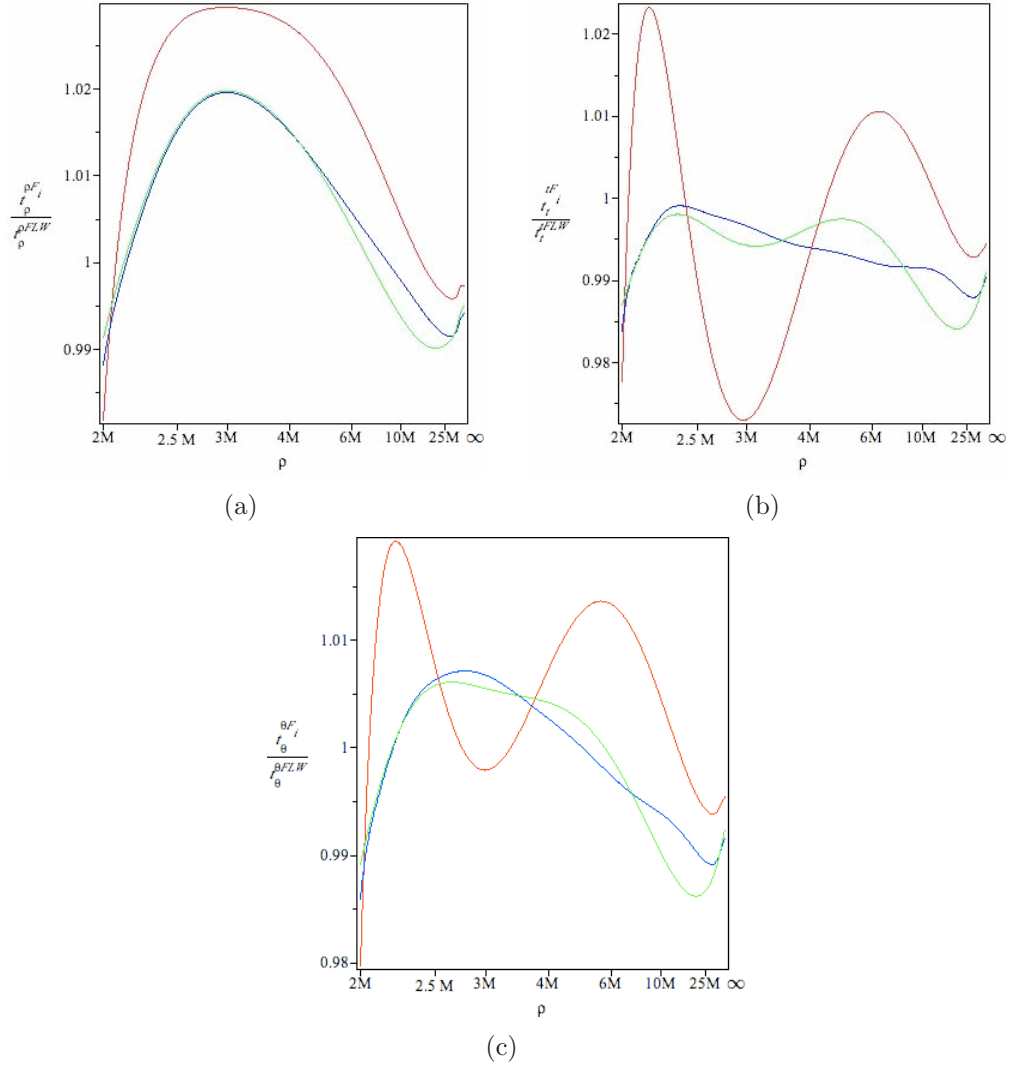
Figure 5.5: The ratios of $t_\mu^{\nu F_{11}}$, $t_\mu^{\nu F_{\mathrm{FLW}}}$, and $t_\mu^{\nu F_{\mathrm{our}}}$ to the FLW data $t_\mu^{\nu \mathrm{FLW}}$. (a) The red, green, and blue lines are the ratios of $t_\rho^{\rho F_{11}}$, $t_\rho^{\rho F_{\mathrm{FLW}}}$, and $t_\rho^{\rho F_{\mathrm{our}}}$ to the FLW data $t_\rho^{\rho \mathrm{FLW}}$, respectively. (b) The red, green, and blue lines are the ratios of $t_t^{t F_{11}}$, $t_t^{t F_{\mathrm{FLW}}}$, and $t_t^{t F_{\mathrm{our}}}$ to the FLW data $t_t^{t \mathrm{FLW}}$, respectively. (c) The red, green, and blue lines are the ratios of $t_\theta^{\theta F_{11}}$, $t_\theta^{\theta F_{\mathrm{FLW}}}$, and $t_\theta^{\theta F_{\mathrm{our}}}$ to the FLW data $t_\theta^{\theta \mathrm{FLW}}$, respectively.

5.2   Comparison of the Metric

The perturbed part of the brane metric (4.7), h_μ^ν, can be calculated by means of equations (4.8)-(4.10). The $h_\rho^{\rho F_{11}}$ derived by using the F_{11} fit is plotted in Fig. 5.6(a), and the ratios of h_ρ^ρ generated by F_{Our}, F_{FLW}, and F_{11} are shown in Fig. 5.6(b). The ratios of the h_ρ^ρ, which involve the derivative of F_i, have deviations from unity up to 9.3%. Therefore, when we are neither near the black hole horizon, $\rho = 2M$ in our gauge, nor near $2M/\rho = 0$, where $h_\rho^\rho = 0$ at both limits, the deviation value of $g_{\rho\rho}$ from the Schwarzschild value cannot be described precisely by our F_{Our}. However, the deviation for the FLW fit from the F_{11} fit is a few percent, which can be an independent confirmation for their result.

Recalling Eq.(4.25), the horizon area is shifted from the Schwarzschild value $A_{Sch} = 4\pi(2M)^2$ to $A_{RSII} = 4\pi[(2M)^2 + F(1)/(-\Lambda)]$, where $F(1)$ is the value of F at $y \equiv 2M/\rho = 1$, on the black hole horizon. The fit to the FLW data gives $F^{FLW}(1) \approx 0.372$, and the fit to our data gives $F^{Our}(1) \approx 0.373$, which shows an agreement within 0.3%. Then, the change from the Schwarzschild black hole to an RSII black hole on the brane with the same ADM mass M increases the horizon by $4.67/(-\Lambda)$ for the FLW fit and by $4.69/(-\Lambda)$ for our fit.

There is one more quantity, the Weyl tensor, that we can use to make another brief comparison. We have used different coordinates for our metric from those used by FLW, which makes comparisons over the entire five-dimensional manifold difficult. The minimum value for the length scale given by the inverse fourth root of the total trace of the square of the Weyl tensor,

$(C_{\alpha\beta\gamma\delta}C^{\alpha\beta\gamma\delta})^{-\frac{1}{4}}$, can be calculated at the corner $x = 1$ and $y = 1$, the intersection of the axis and the black hole horizon. The value for our metric is 0.206 and for the FLW metric is 0.198, which are within 4% of each other.

(a)   (b)
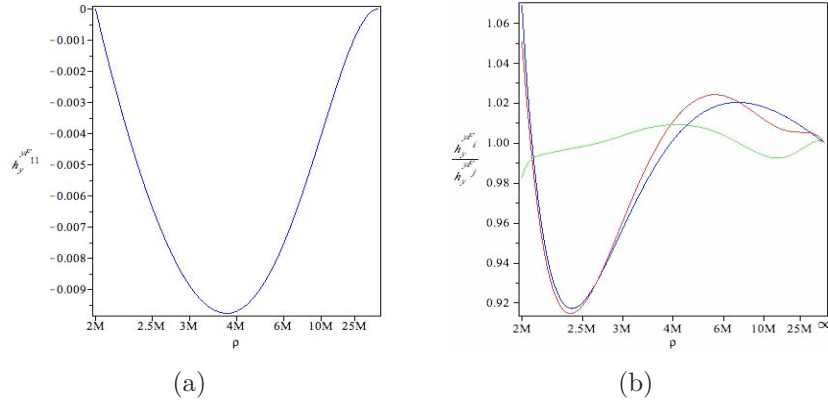
Figure 5.6: (a) $h_\rho^{\rho F_{11}}$. (b) The blue, green, and red curves are the ratios $\dfrac{h_\rho^{\rho F_{\text{our}}}}{h_\rho^{\rho F_{\text{FLW}}}}$, $\dfrac{h_\rho^{\rho F_{\text{our}}}}{h_\rho^{\rho F_{11}}}$, and $\dfrac{h_\rho^{\rho F_{\text{FLW}}}}{h_\rho^{\rho F_{11}}}$, respectively.

(a)   (b)
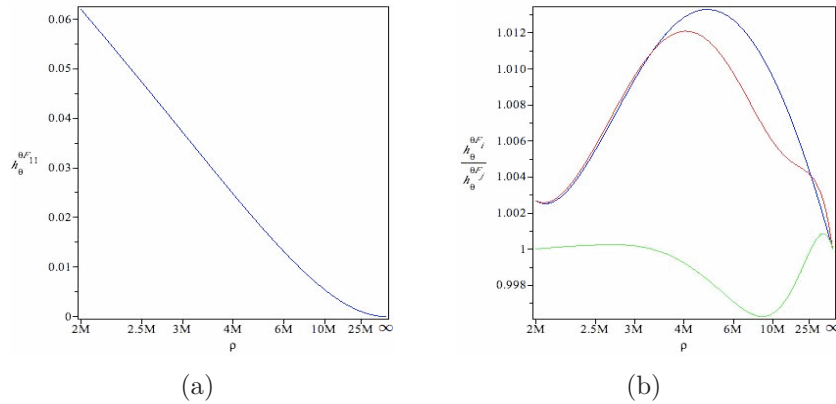
Figure 5.7: (a) $h_\theta^{\theta F_{11}}$. (b) The blue, green, and red curves are the ratios $\dfrac{h_\theta^{\theta F_{\text{our}}}}{h_\theta^{\theta F_{\text{FLW}}}}$, $\dfrac{h_\theta^{\theta F_{\text{our}}}}{h_\theta^{\theta F_{11}}}$, and $\dfrac{h_\theta^{\theta F_{\text{FLW}}}}{h_\theta^{\theta F_{11}}}$, respectively.

Therefore, we have shown that all plots and results that we can derive from FLW and our data are in a close agreement. So, this can be considered as a good confirmation for the existence of the large black hole in RSII.

Chapter 6

Conclusion

We can consider the RSII braneworld model as a good candidate for describing our four-dimensional universe, the brane, with an extra dimension, in which the four-dimensional physics is recovered on the brane. We probe the existence of large black holes for the RSII model. Because of the astrophysical observation of such black holes, the non-existence of large black holes in the RSII model would be strong evidence against the practicality of the model. On the other hand, a black hole in the RSII model can be different from a black hole in four-dimensional general relativity, so it might be a good opportunity to study the extra dimension using astronomical observations of black holes.

We have constructed a large black hole solution in the RSII model numerically in two steps. First, an infinite-mass black hole has been found by using a spectral method to minimize the integral of the squared error for the Einstein equation, with four free functions to be found and 210 parameters to vary. For the next step, the perturbation has been applied to move the

location of the brane from infinity and find the large black hole. Finally, we have derived a closed-form approximation metric, (4.12), for the black hole on the brane.

We also have concluded that to the first order in our perturbation parameter $1/(-\Lambda M^2)$, the Hawking temperature and entropy of the derived black hole is the same as the Schwarzschild black hole with the same ADM mass M. But, the black hole horizon area is increased by $4.69/(-\Lambda)$ from the Schwarzschild black hole horizon area with mass M.

Figueras, Lucietti, and Wiseman have found a large black hole solution in RSII. Our approach to the problem is independent from the FLW approach. FLW solved the full non-linear Einstein equation with the brane boundary condition. But, we solved the problem by a perturbative approach, which is a distinct and original way to find the large black hole in RSII. We have provided evidence in support of the FLW result by comparing their numerical results to ours. We have found the fitting functions (5.4) and (5.5), respectively to our data and their data, and we have shown that our results agree, within numerical errors, with theirs.

The large black hole that we have found is quite close to the Schwarzschild black hole, and this solution can lead us to still consider the RSII model as a possible candidate for describing our universe in a model including extra dimension.

Bibliography

[1] S. Abdolrahimi, C. Cattoën, D. N. Page, and S. Yaghoobpour-Tari, arXiv:1206.0708v3[hep-th], (2012).

[2] S. Abdolrahimi, C. Cattoën, D. N. Page, and S. Yaghoobpour-Tari, Extension upon [1], in preparation.

[3] O. Aharony, S. S. Gubser, J. M. Maldacena, H. Ooguri, and Y. Oz, Phys. Rep. **323**, 183 (2000).

[4] N. Arkani-Hamed, S. Dimpoulos, and G. R. Dvali, Phys. Lett. B **429**, 263 (1998).

[5] N. Arkani-Hamed, S. Dimpoulos, and G. R. Dvali, Phys. Rev. D **59**, 086004 (1999).

[6] A. R. Bogojevic and L. Perivolaropoulos, Mod. Phys. Lett. A **6**, 369 (1991).

[7] M. Cavaglia, Int. J. Mod. Phys. A **18**, 1843 (2003).

[8] A. Chamblin, S. W. Hawking, and H. S. Reall, Phys. Rev. D **61**, 065007 (2000).

[9] K. Cheung, arXiv: hep-ph/0305003 e-print, (2003).

[10] S. Dimopoulos and G. L. Landsberg, Phys. Rev. Lett. **87**, 161602 (2001).

[11] R. Emparan, A. Fabbri, and N. Kaloper, JHEP **08**, 043 (2002).

[12] R. Emparan, J. Garcia-Bellido, and N. Kaloper, JHEP **0301**, 079 (2003).

[13] R. Emparan, G. T. Horowitz, and R. C. Myers, J. High Energy Phys. **01**, 007 (2000).

[14] R. Emparan and H. S. Reall, Living Rev. Rel. **11**, 6 (2008).

[15] C. Fefferman and C. R. Graham,*Conformal invariants*, Élie Cartan et les Math ématiques dáujourd'hui, Astérisque, hors série, Soc. Math. France, Paris, 95 (1985).

[16] P. Figueras, J. Lucietti, and T. Wiseman, Class. Quantum Grav. **28**, 215018 (2011).

[17] P. Figueras and T. Wiseman, Phys. Rev. Lett. **107**, 081101 (2011).

[18] A. L. Fitzpatrick, L. Randall, and T. Wiseman, JHEP **11**, 033 (2006).

[19] A. V. Frolov and V. P. Frolov, Phys. Rev. D **67**, 124025 (2003).

[20] V. P. Frolov and D. Stojkovic, Phys. Rev. Lett **89**, 151302 (2002).

[21] V. P. Frolov and D. Stojkovic, Phys. Rev. D **67**, 084004 (2003).

[22] V. P. Frolov and A. Zelnikov, *Introduction to Black Hole Physics*, Oxford University Press, UK, (2011).

[23] J. Garriga and T. Tanaka, Phys. Rev. Lett. **84**, 2778 (2000).

[24] S. B. Giddings and S. Thomas, Phys. Rev. D **65**, 056010 (2002).

[25] C. R. Graham, *Volume and Area Renormalizations for Conformally Compact Einstein Metrices*, 19th Winter School on Geometry and Physics, Srni, Czech Republic, (1999), arXiv:math/9909042[math-dg].

[26] C. R. Graham and J.M. Lee, Adv. Math. **87**, 186 (1991).

[27] R. Gregory and R. Laflamme, Phys. Rev. Lett.**70**, 2837 (1993).

[28] R. Gregory and R. Laflamme, Nucl. Phys. B **428**, 399 (1994).

[29] S. de Haro, S. N. Solodukhin, and K. Skenderis, Commun. Math. Phys. **217**, 595 (2001).

[30] M. Headrick, S. Kitchen, and T. Wiseman, Class. Quant. Grav. **27**, 035002 (2010).

[31] G. T. Horowitz and T. Wiseman, arXiv:1107.5563v2 e-print, (2011).

[32] C. D. Hoyle, U. Schmidt, B. R. Heckel, E. G. Adelberger, J. H. Gundlach, D. J. Kapner, and H. E. Swanson, Phys. Rev. Lett. **86**, 1418 (2001).

[33] W.Israel, Nuova Cim B **44**, (1966).

[34] T. Kaluza, Sitzungsber. Preuss. Akad. Wiss. Berlin, Phys. Math. Kl, 996 (1921).

[35] P. Kanti, Int. J. Mod. Phys. A **19**, 4899 (2004).

[36] D. Karasik, C. Sahabandu, P. Suranyi, and L. C. R. Wijewardhana, Phys. Rev. D **70**, 064007 (2004).

[37] A. Kaus and H. S. Reall, J. High Energy Phys. **05**, 032 (2009).

[38] W. Kinnersley and M. Walker, Phys. Rev. D **2**, 1359 (1970).

[39] O. Klein, Z. F. Physik **37**, 895 (1926).

[40] H. Kudoh, Phys. Rev. D **69**, 104019 (2004).

[41] H. Kudoh, T. Tanaka ,and T. Nakamura, Phys. Rev. D **68**, 024035 (2003).

[42] H. Kudoh and T. Wiseman, Prog. Theor. Phys. **111**, 475 (2004).

[43] H. K. Kunduri, J. Lucietti, and H. S. Reall, Class. Quant. Grav. **24**, 4169 (2007).

[44] J.C. Lagarias, J. A. Reeds, M. H. Wright, and P. E. Wright, SIAM Journal of Optimization **9**, (1998).

[45] R. Maartens and K. Koyama, Living Rev. Relativity **13**, 5 (2010).

[46] J. M. Maldacena, Adv. Theor. Math Phys. **2**, 231 (1998).

[47] D. Marolf, Gen. Rel. Grav. **41**, 903 (2009).

[48] R. C. Myers and M. J. Perry, Annals Phys. **172**, 304 (1986).

[49] G. Nordström, Phys. Zeitschr **15**, 504 (1914).

[50] J. F. Plebanski and M. Demianski, Ann. Phys. **98**, 98 (1976).

[51] E. Poisson, *A Relativist's Toolkit: The Mathematics of Black-Hole Mechanics*, Cambridge University Press, UK, (2004).

[52] L. Randall and R. Sundrum, Phys. Rev. Lett. **83**, 3370 (1999).

[53] L. Randall and R. Sundrum, Phys. Rev. Lett. **83**, 4690 (1999).

[54] V. A. Rubakov and M. E. Shaposhnikov, Phys. Lett. B **125**, 136 (1983).

[55] L. F. Shampine, Applied Mathematics and Computation **202**, (2008).

[56] T. Shiromizu, K. Maeda and M. Sasaki, Phys. Rev. D **62**, 024012 (2000).

[57] A. Strominger and C. Vafa, Phys. Lett. B **379**, 99 (1996).

[58] N. Tanahashi and T. Tanaka, Prog. Theor. Phys. Suppl. **189**, 227 (2011).

[59] T. Tanaka, Prog. Theor. Phys. Suppl. **148**, 307 (2003).

[60] F. R. Tangherlini, Nuovo Cim. **27**, 636 (1963).

[61] R. M. Wald, *General Relativity*, Uni. Chicago Press, Chicago, (1984).

[62] T. Wiseman, Phys. Rev. D **65**, 124007 (2002).

[63] H. Yoshino, J. High Energy Phys. **01**, 068 (2009).

Appendix A

The Numerical Results for Metric Functions

The functions $A(x,y)$, $B(x,y)$, $C(x,y)$ and $D(x,y)$ in the metric (3.3), after numerically minimizing the integral of the squared error (3.13) by 6th order polynomials with 210 coefficients are given by the following expressions, with all of the coefficients rounded to five digits after the decimal place:

$$
\begin{aligned}
A(x,y) \;=\; & 1 + (0.21094 + 0.95771y - 0.32215y^2 + 0.07863y^3 \\
& - \;\; 0.14553y^4 + 0.08707y^5 - 0.00708y^6)x \\
& + \;\; (0.483120 - 2.96522y + 3.12221y^2 + 1.58758y^3 \\
& - \;\; 3.26594y^4 + 1.42017y^5 - 0.15995y^6)x^2 \\
& + \;\; (-1.71060 + 15.96474y - 30.20818y^2 + 13.67479y^3 \\
& + \;\; 7.52368y^4 - 6.45629y^5 + 0.54667y^6)x^3
\end{aligned}
$$

$$+ \quad (5.78445 - 61.41107y + 170.77950y^2 - 214.55752y^3$$

$$+ \quad 153.70395y^4 - 73.81142y^5 + 20.14974y^6)x^4$$

$$+ \quad (-11.34737 + 143.59002y - 527.23697y^2 + 941.06600y^3$$

$$- \quad 951.41715y^4 + 539.77303y^5 - 135.40474y^6)x^5$$

$$+ \quad (14.60367 - 212.76740y + 940.10896y^2 - 2014.17705y^3$$

$$+ \quad 2340.50264y^4 - 1423.20017y^5 + 356.46300y^6)x^6$$

$$+ \quad (-11.53285 + 191.11234y - 965.53690y^2 + 2306.98150y^3$$

$$- \quad 2889.53569y^4 + 1827.70113y^5 - 460.15121y^6)x^7$$

$$+ \quad (5.01719 + -94.50791y + 529.64141y^2 - 1357.87635y^3$$

$$+ \quad 1776.26250y^4 - 1148.20207y^5 + 289.36969y^6)x^8$$

$$+ \quad (-0.90738 + 19.65670y - 120.15064y^2 + 323.38343y^3$$

$$- \quad 433.62615y^4 + 282.63877y^5 - 70.80546y^6)x^9, \tag{A.1}$$

$$
\begin{aligned}
B(x,y) \quad = \quad & 1 + (-0.60547 - 0.47885y + 0.16108y^2 - 0.03931y^3 \\
& + \quad 0.07277y^4 - 0.04354y^5 + 0.003540y^6)x \\
& + \quad (0.43149 - 0.80874y + 0.89420y^2 - 0.31160y^3 \\
& - \quad 0.09760y^4 + 0.08441y^5 - 0.00482y^6)x^2 \\
& + \quad (0.21851 + 0.08687y - 1.72664y^2 + 2.47145y^3 \\
& - \quad 0.92513y^4 - 0.07910y^5 + 0.05733y^6)x^3 \\
& + \quad (-0.24942 + 0.72759y + 3.13465y^2 - 9.10834y^3 \\
& + \quad 8.03309y^4 - 3.11900y^5 + 0.42049y^6)x^4
\end{aligned}
$$

$$+ \quad (0.11567 + 0.85762y - 8.90011y^2 + 22.33435y^3$$

$$- \quad 24.96171y^4 + 13.30179y^5 - 2.72886y^6)x^5$$

$$+ \quad (0.11933 - 2.07556y + 11.88780y^2 - 30.32368y^3$$

$$+ \quad 37.81788y^4 - 22.84820y^5 + 5.46718y^6)x^6$$

$$+ \quad (-0.03621 + 0.99966y - 7.11882y^2 + 20.49026y^3$$

$$- \quad 28.00052y^4 + 18.39565y^5 - 4.74288y^6)x^7$$

$$+ \quad (0.00555 - 0.20539y + 1.74472y^2 - 5.66200y^3$$

$$+ \quad 8.40417y^4 - 5.81216y^5 + 1.52634y^6)x^8, \qquad\qquad \text{(A.2)}$$

$$
\begin{aligned}
C(x,y) \quad = \quad & 1 + (-0.60547 - 0.47885y + 0.16108y^2 - 0.03931y^3 \\
+ \quad & 0.07277y^4 - 0.04353y^5 + 0.00354y^6)x \\
+ \quad & (-0.14516 + 1.32670y - 1.67755y^2 + 0.52746y^3 \\
+ \quad & 0.82884y^4 - 1.10767y^5 + 0.49529y^6 - 0.06057y^7)x^2 \\
+ \quad & (0.27707 - 2.97720y + 6.80878y^2 - 6.66724y^3 \\
+ \quad & 2.34156y^4 + 2.29259y^5 - 2.95084y^6 + 0.978589y^7)x^3 \\
+ \quad & (-0.54534 + 5.46359y - 13.40233y^2 + 12.20018y^3 \\
+ \quad & 3.69101y^4 - 21.56518y^5 + 20.75440y^6 - 6.75727y^7)x^4 \\
+ \quad & (0.63505 - 6.58020y + 16.26668y^2 - 7.88244y^3 \\
- \quad & 32.05193y^4 + 69.62487y^5 - 57.58350y^6 + 17.59022y^7)x^5 \\
+ \quad & (-0.42810 + 5.02395y - 14.87309y^2 + 10.13469y^3 \\
+ \quad & 30.26574y^4 - 73.46057y^5 + 62.70428y^6 - 19.32214y^7)x^6
\end{aligned}
$$

$$
\begin{aligned}
&+ \quad (0.15406 - 2.23357y + 9.56540y^2 - 15.94279y^3 \\
&+ \quad 4.13362y^4 + 20.02335y^5 - 24.13180y^6 + 8.41885y^7)x^7 \\
&+ \quad (-0.01891 + 0.44363y - 2.86261y^2 + 7.61814y^3 \\
&- \quad 9.31272y^4 + 4.24741y^5 + 0.75762y^6 - 0.87134y^7)x^8,
\end{aligned}
\tag{A.3}
$$

$$
\begin{aligned}
D(x,y) \;=\; & 1 + (0.39453 - 0.47885y + 0.16108y^2 - 0.03931y^3 \\
&+ \quad 0.07276y^4 - 0.04354y^5 + 0.00354y^6)x \\
&+ \quad (0.05130 + 0.60697y - 0.17110y^2 - 1.10809y^3 \\
&+ \quad 1.02899y^4 - 0.23688y^5 - 0.02783y^6)x^2 \\
&+ \quad (0.32335 - 2.49967y + 5.37277y^2 - 6.15484y^3 \\
&+ \quad 7.81122y^4 - 7.43134y^5 + 2.80293y^6)x^3 \\
&+ \quad (-0.52530 + 7.18773y - 31.23730y^2 + 79.39889y^3 \\
&- \quad 119.57662y^4 + 94.40212y^5 - 29.80903y^6)x^4 \\
&+ \quad (0.58030 - 12.77895y + 87.87779y^2 - 284.24264y^3 \\
&+ \quad 463.83801y^4 - 369.81230y^5 + 115.08588y^6)x^5 \\
&+ \quad (-0.13189 + 14.60642y - 144.69672y^2 + 529.23363y^3 \\
&- \quad 899.73602y^4 + 725.67077y^5 - 225.66361y^6)x^6 \\
&+ \quad (-0.30734 - 11.10747y + 144.89421y^2 - 565.76399y^3 \\
&+ \quad 982.58529y^4 - 797.70747y^5 + 248.00979y^6)x^7 \\
&+ \quad (0.29947 + 5.31976y - 82.06726y^2 + 330.24011y^3 \\
&- \quad 579.34304y^4 + 472.44205y^5 - 147.08568y^6)x^8
\end{aligned}
$$

$$+ \quad (-0.08325 - 1.22603y + 20.06377y^2 - 81.40275y^3$$

$$+ \quad 143.32172y^4 - 117.33319y^5 + 36.68467y^6)x^9. \qquad \text{(A.4)}$$

Note that after plugging the 6th order polynomials with (3.23)-(3.28), the polynomials A, B, C, and D end up having slightly higher order and 249 coefficients with 39 of them not independent.